Study of industrial titania synthesis using a hybrid particle-number and detailed particle model

Astrid Boje[a,b], Jethro Akroyd[a,b], Stephen Sutcliffe[d], Markus Kraft[a,b,c,*]

[a]*Department of Chemical Engineering and Biotechnology, University of Cambridge, West Cambridge Site, Philippa Fawcett Drive, Cambridge CB3 0AS, United Kingdom*
[b]*CARES, Cambridge Centre for Advanced Research and Education in Singapore, 1 Create Way, CREATE Tower, #05-05, Singapore, 138602*
[c]*School of Chemical and Biomedical Engineering, Nanyang Technological University, 62 Nanyang Drive, Singapore, 637459*
[d]*Formerly at Venator, Titanium House, Hanzard Drive, Wynyard Park, TS22 5FD, United Kingdom*

Abstract

We apply a hybrid particle model to study synthesis of particulate titania under representative industrial conditions. The hybrid particle model employs a particle-number description for small particles, and resolves complicated particle morphology where required using a detailed particle model. This enables resolution of particle property distributions under fast process dynamics. Robustness is demonstrated in a network of reactors used to simulate the industrial process. The detailed particle model resolves properties of the particles that determine end-product quality and post-processing efficiency, including primary particle size and degree of aggregate cohesion. Sensitivity of these properties to process design choices is quantified, showing that higher temperature injections produce more sintered particles; more frequent injections narrow the geometric standard deviation of primary particle diameter; and chlorine dilution reduces particle size and

*Corresponding author
Email address: mk306@cam.ac.uk (Markus Kraft)

size variance. Structures of a typical industrial particle are compared visually with simulated particles, illustrating similar aggregate features with slightly larger primary particles.

Keywords: titanium dioxide, detailed particle model, particle-number model, high rate, particle processes, population balance

1. Introduction

Understanding aerosol synthesis of particulates is challenging due to the complex interactions between chemistry, heat transfer, fluid dynamics and particle structure, with particle size and morphology determined by process conditions. In particular, control of heat transfer and reaction processes is central to producing desired product structure in a process that typically generates non-spherical, fractal-like aggregates [1, 2]. Need to target specific product properties has motivated extensive study – see, for example, the review of Li et al. [3]. Synthesis of pigmentary titanium dioxide (TiO_2, titania) by the chloride process [4] is a salient example and will be the focus of this paper.

Titanium dioxide is an important industrial product, with applications spanning pigments [5] to photocatalytics [6, 7]. TiO_2 powder is produced on the scale of millions of tons per annum [8] and aerosol synthesis via the chloride process accounts for approximately 60 % of white pigmentary TiO_2 [1]. The opacity of the product is governed by the size and morphology of the pigment particles – thus understanding of the synthesis is crucial as it can minimise expensive post-processing steps such as milling to achieve suitable sizes [9, 10].

Experimental studies and acquisition of plant data are hindered by elevated temperatures and pressures (>1000 K and several bar), residences times in the

order of milliseconds and the chlorine environment. However, useful laboratory studies exist, including the early thin film studies of Ghoshtagore [11] and hot wall reactor of Pratsinis et al. [12] as well as many more recent results [13, 14, 15, 16]. In addition to allowing direct study of particulate properties, for example by imaging, such studies provide a means of testing and building numerical models [17, 18, 19] which allows for rapid investigation of process conditions that are expensive/challenging to realize experimentally.

Numerical studies require (i) a model for the particle type space, i.e. the mathematical description of possible particle properties; (ii) a mechanism for formation and growth processes, possibly combined with chemical kinetics for the gas-phase and heat/transport processes; (iii) a numerical method with which to solve these constituent equations. Type space models can be characterised as spherical [20], surface area/volume [21] and detailed [22, 23], with increasing complexity attributed to particle models with more dimensions/internal coordinates [24]. Detailed models are required to describe polydisperse particle populations and systems with similar coagulation and sintering timescales [25].

Popular numerical methods for solving population balance equations include moment-based [26, 27, 28], sectional [29, 30, 31] and Monte Carlo [32, 33, 34, 35, 36, 37] treatments [38]. Although other methods can be optimised to accommodate several particle internal coordinates [39], the stochastic approach is necessary when a detailed particle model is used as this can extend to thousands of internal coordinates (resolving particle connectivity as well as sizes). Direct simulation with a detailed particle model has been used to study titania synthesis in previous work e.g. [40, 41], including studies that specifically targeted understanding of industrially-relevant conditions using simpler particle [42] and flow [43] models

respectively. These studies highlighted the high computational cost of simulating high-rate conditions.

In recent work [44], we proposed a new algorithm for a hybrid particle type space model, termed the particle-number/particle (PN/P) model, in the spirit of the approach of Babovsky [45], and demonstrated its improvement of the efficiency and robustness of direct simulation under high-rate conditions. The PN/P model supports the stochastic algorithm under conditions of rapid particle formation and growth by tracking newly incepted primary particles separately, freeing up space in the discrete particle ensemble for resolving aggregates with a detailed particle model. This is in contrast to the hybrid approach proposed by Bouaniche et al. [46] recently, which resolves the full particle size distribution (PSD) using sectional and stochastic approaches to treat artificial diffusion for high growth rates. The current work incorporates the new overlapping spheres, primary coordinate tracking, particle model of Lindberg et al. [23] which provides further resolution in the particle type space and eliminates assumptions on fractal dimension in calculating particle collision rates.

The **purpose of this work** is to develop new understanding of the particle structures formed in industrial titania synthesis by combining two recently introduced models: a more detailed particle model including primary coordinate tracking; and a hybrid particle type space model that allows more efficient, robust simulation of the industrial process. We revisit the reactor network approach [47] for modelling the industrial reactor [43], including an energy balance to extend applicability to a wider range of configurations and operating conditions. The PN/P model is used to handle rapid particle inception under the industrial conditions and the detailed particle model is used to describe complex aggregate structures that

develop due to coagulation and surface processes with sufficient detail to compare with features of the industrial product.

This paper is **structured as follows**: important features of the particle models and processes are outlined in Sections 2.1 and 2.2 respectively. The modelling section ends with a description of the reactor model in Section 2.3, including relevant mass and energy balance equations (2.3.1) and details with motivation for the cases to be considered (2.3.2). The numerical method is discussed in Section 3, which highlights new features (3.1), lists parameters (3.2) and illustrates performance (3.3). Results follow in Section 4, covering an investigation of particle structure for base case conditions (4.1), a study of sensitivity of particle structure to alternate process design choices (4.2), characterisation of fractal structure (4.3), and comparison of visualisations of particle geometry (4.4). Finally, conclusions are stated in Section 5.

2. Model description

2.1. Particle models

The particle model is a key ingredient in the modelling framework because it determines the maximum amount of information that can be obtained directly about product morphology without requiring further assumptions on shape. We consider modelling particles at two levels: primary particles (primaries), which consist of chemically bonded units of TiO_2 and are described by the number of atoms they contain, and aggregate particles which are formed from multiple, independently-tracked primaries with arbitrary connectivity. The particle type space provides a mathematical description of the particles: a particle has type $x \in \mathcal{E}$, where $\mathcal{E}$ includes descriptions of all possible particles. This paper uses a

hybrid particle-number/particle (PN/P) model [44] which splits the particle type space into small primary particles, $x \in \mathcal{M} \subset \mathcal{E}$, and large/complex particles, $x \in \mathcal{X} \subset \mathcal{E}$, (Fig. 1). Different levels of detail are required to describe particles in each sub-space.

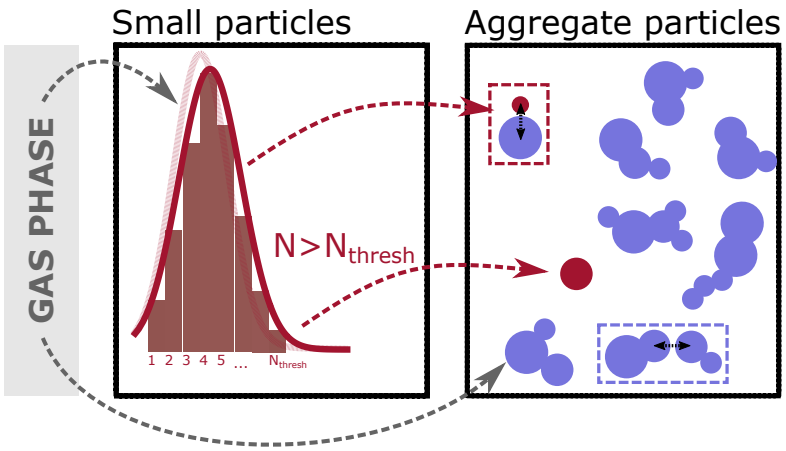

Figure 1: Hybrid particle state space showing mass transfer between the gas-phase and the particle systems and between the space of small primary particles with size less than N_{thresh} and the space of aggregate particles [44].

2.1.1. Particle-number model

In the particle-number type space, $\mathcal{M}$, particles consist of only one primary particle, p_i, defined by a single internal coordinate, η_i, which tracks the number of units of the chemical species contained,

$$p_i = p_i(\eta_i)\,. \tag{1}$$

For titania, η tracks the number of TiO_2 molecules making up the primary particle (Fig. 2(a)). Only particles smaller than a threshold size of N_{thresh} are de-

scribed by the particle-number model, i.e. $x \in [1, N_{\text{thresh}}]$. Particles are modelled as spheres, thus the diameter of a particle d_{p} can be computed from its mass m,

$$m(p_i) = \frac{\eta_i \text{MW}}{N_{\text{A}}} \implies d_{\text{p}}(p_i) = \left(\frac{6}{\pi} \frac{m(p_i)}{\rho} \right)^{1/3}. \tag{2}$$

Here, N_{A} is Avogadro's constant and the first expression converts the number of molecules tracked by η_i to moles and multiplies by the molecular mass, MW, to yield mass. The second expression converts mass to volume and thus finds the sphere-equivalent diameter using the particle mass density, ρ.

2.1.2. Detailed particle model

The detailed particle type space, $\mathcal{X}$, describes primary particles larger than the threshold and particles with more complex morphology. A particle, P_q, is modelled by a list of constituent primary particles, p_i, $i = 1, \ldots, n_q$, and a data structure, $\mathbf{C}_q$,

$$P_q = P_q\left(p_1, \ldots, p_{n_q}, \mathbf{C}_q\right). \tag{3}$$

$\mathbf{C}_q$ tracks the connectivity of the primary particles i.e. which primary particles are adjacent in the aggregate. The value of each element, $C_{ij} \in \mathbf{C}_q$, depends on the relative positions of primary particles p_i and p_j (see Fig. 2(b)),

$$C_{ij} = \begin{cases} 1 & \text{if } p_i, p_j \text{ are adjacent} \\ 0 & \text{if } p_i, p_j \text{ are not adjacent.} \end{cases} \tag{4}$$

Primary particles p_i are described by their chemical composition η_i, their radius r_i and their position $\mathbf{z}_i$,

$$p_i = p_i\left(\eta_i, r_i, \mathbf{z}_i\right). \tag{5}$$

The coordinates $\mathbf{z}_i$ specify the location of the primary centre relative to the centre of mass of the aggregate. This informs the centre-to-centre separation d_{ij},

$$d_{ij} = \left|\mathbf{z}_i - \mathbf{z}_j\right|, \tag{6}$$

which measures the degree of overlap between adjacent primary particles. The coordinates also specify the centre-to-neck distance x_{ij} and the radius of the neck r_{ij} between adjacent primaries p_i and p_j (see Fig. 2(c)). Extensive detail for computing these particle properties is provided in the paper by Lindberg et al. [23].

The primary coordinates can also be used to compute the diameter of gyration, and thus the collision diameter d_c,

$$d_\mathrm{c}\left(P_q\right)^2 = \frac{4}{\sum_{i=1}^{n_q} m\left(p_i\right)} \sum_{i=1}^{n_q} m\left(p_i\right)\left(\left|\mathbf{z}_i\right|^2 + r_i^2\right), \tag{7}$$

can be defined without assuming a particular fractal structure to relate the aggregate composition to its size [23].

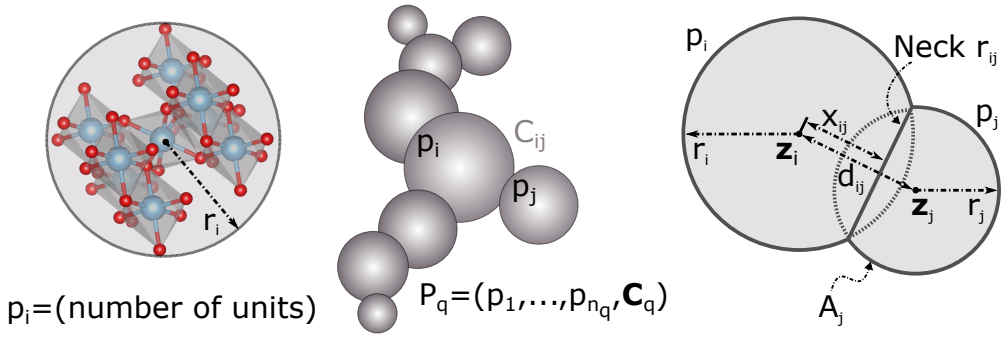

(a) Solo primary particle (b) Detailed particle model (c) Primary connectivity

Figure 2: TiO_2 primary particle p_i defined by its chemical composition with volume-equivalent radius r_i. Particle, P_q, is composed of a list of primaries, p_i, connected as overlapping spheres according to their relative 3D coordinates $\mathbf{z}_i$, with tracking of radii, separation distances and surface area [23].

2.2. Particle processes

The evolution of a particle population is governed by several formation and growth processes. This work studies the chloride synthesis of TiO_2, for which the important particle processes are inception, surface growth, coagulation and sintering (described in Sections 2.2.1–2.2.4). The inception and surface growth processes transfer mass from the gas-phase, following decomposition and/or oxidation of the precursor $TiCl_4$. In this work, the gas-phase mechanism developed by West et al. [40, 48], with subsequent extensions [49, 50, 51], is used to describe the decomposition of the precursor, oxidation to form titanium oxychlorides, and chlorine chemistry. The mechanisms for the particle processes have also been described in much detail in previous publications, both for titania [40, 42, 41, 43, 23, 44], and for other systems [52, 53, 22]; thus, only important features are mentioned here. This work extends the energy balance presented by

Celnik et al. [34] to include heat release by particle processes in order to study the exothermic process under conditions with more significant solid fractions.

2.2.1. Inception

Inception is the process by which particles form in the solid phase following collision between gas-phase species. The inception mechanism used in this work includes 105 bimolecular collision reactions between titanium oxychlorides, producing a new spherical primary particle as in [42, 40]. The numerical inception rate, I, is informed by the collision rate for the free molecular regime. Inception alters the system temperature by heat of gas-phase reaction and formation of the new particle surface.

Inception increases the particle-number count, adding a particle of type $x_{\text{inc}} \in \mathcal{M}$ which is modelled by increasing the count at size η_{inc}, where η_{inc} refers to the number of TiO_2 units in the new particle. Because the primary particle model is univariate, this treatment is exact compared to the single type space modelling approach [44].

2.2.2. Surface growth

Surface growth refers to the addition of mass to the surface of an existing particle by direct oxidation of $TiCl_4$, with the reaction rate assumed to be first order in $TiCl_4$ and O_2 as in Akroyd et al. [42], with constants fitted from the hot wall reactor experiments of Pratsinis et al. [12] by Lindberg et al. [41]. Surface growth also contributes to the energy balance by exothermic gas-phase reaction and formation of new particle surface.

For particles described by the particle-number model with η_i units, surface growth is simply the addition of η_{add} new units, modelled by increasing the count

at size $\eta_i + \eta_{\text{add}}$ and decreasing the count at size η_i [44]. Surface growth is more complex for aggregate particles since the addition of η_{add} units changes the relative centres of mass of the primaries and the primary separations, requiring the adjustments described by Lindberg et al. [23].

2.2.3. Coagulation

Coagulation is a collision process after which particles remain in lasting point contact. Coagulation is treated as addition in the combined type space:

$$P(x) + P(y) \rightarrow P(x + y), \ (x, y) \in \mathcal{E}. \tag{8}$$

Coagulation is modelled using a ballistic cluster-cluster algorithm (BCCA) with a random impact parameter as outlined by Lindberg et al. [23]. The collision direction is specified by random choice of: rotation around the centre of mass of each particle and surface point for contact on one of the particles. The random impact is applied by placing the second particle at an arbitrary position in the plane perpendicular to the collision direction. And the rate is informed by the coagulation kernel for the transition regime [44].

A particle tracked by the particle-number model is transferred to the detailed particle model when it coagulates with any other particle, i.e. the coagulation kernel $K : \mathcal{E}^2 \rightarrow \mathcal{X}$.

2.2.4. Sintering

Sintering describes the growth of 'necks' between adjacent primaries as their degree of overlap increases. For TiO_2, the dominant mechanism is grain boundary diffusion [54]. Sintering reduces the centre-to-centre distance between primaries,

with increase in the primary radii and centre-to-centre distance of neighbouring pairs to conserve mass. The equations for how these properties alter as particles sinter are provided by Lindberg et al. [23]. The extent of sintering is assessed in term of the 'sintering level',

$$s_{ij} = \frac{r_{ij}}{r_j}, \quad r_j \leq r_i, \tag{9}$$

where r_{ij} is the radius of the neck connecting primaries i and j and the sintering level is defined as the ratio of this neck to the radius of the smaller of the two primary particles.

In theory, sintering also contributes to the heat flux because the surface tension changes as the particles sinter [55, 56]; and this phenomenon is particularly important when particles are very small (less than 10 nm [57]) because the heat loss warms the particle surface, causing it to behave more like a liquid and sinter more rapidly. Here, we stipulate a minimum diameter of $d_{\mathrm{p,min}} = 4\,\mathrm{nm}$ [23, 1] which increases the sintering rate for the smallest particles. We also assume that primary particle pairs coalesce (forming a fully-sintered/single-primary particle) if their sintering level exceeds 0.95 [23].

2.2.5. Flow

Particles also transit through the system by inflow/outflow [47] and this can contribute mixing heat flux. Particle addition/removal effects both type spaces equally, with particle flow increasing/decreasing the count at a given index for the particle-number model and producing/eliminating ensemble particles for the particle model respectively [44].

2.3. Reactor model

The industrial titania reactor consists of a dosing zone to which a roughly equimolar feed of reactants (TiO_2 and O_2) is injected stage-wise, perpendicular to the flow; a working zone where reactions are completed; and a cooling zone or external cooler where the temperature is reduced to minimise particle aggregation and sintering. Hot O_2 gas, supplied at the reactor inlet, is used to aid initial endothermic decomposition of the precursor.

We employ a reactor network approach to model the system, as in previous work [43]. This includes continuously stirred tank reactors (CSTRs) in series with one reactant injection per CSTR 'stage' for the dosing zone, and subsequent plug flow reactors (PFRs) for the tubular working and cooling zones. The previous work modelled the reactor isothermally, with a stipulated temperature profile in the working zone to model completion of the exothermic reactions. This limited the model's flexibility and constrained investigation of different design choices. This motivated the inclusion of the energy balance in the current work where the intention is to investigate process conditions and reactor configurations, such as stream temperatures and dosing strategies respectively.

2.3.1. System equations

For each CSTR with characteristic residence time τ_{CSTR}, the two-phase system including gas-phase reactants, intermediates and byproducts, and solid-phase particulate product is described by coupled equations for the change in number density $n(x)$ of particles of type x, the change in concentration C_k of gas-phase species k, and the change in temperature T due to both reactions and flow. In the following formulation, phase coupling includes gas-phase expansion with the expansion coefficient Γ [34, 47].

The particle number density evolves according to the population balance equation,

$$\begin{aligned}\frac{\mathrm{d}n\left(x\right)}{\mathrm{d}t} =& I\left(x,\mathbf{C},T\right) + \frac{1}{2}\sum_{\substack{y,z\in\mathcal{E}:\\ y+z=x}} K\left(y,z\right)n\left(y\right)n\left(z\right) - \sum_{y\in\mathcal{E}} K\left(x,y\right)n\left(x\right)n\left(y\right) \\ &+ \sum_{\substack{y\in\mathcal{E}:\\ g_{\mathrm{SG}}(y)=x}} \beta_{\mathrm{SG}}\left(y,\mathbf{C},T\right)n\left(y\right) - \beta_{\mathrm{SG}}\left(x,\mathbf{C},T\right)n\left(x\right) \\ &+ \frac{1}{\tau_{\mathrm{CSTR}}}\sum_{j=1}^{N_{\mathrm{in}}} f^{[j]}\left(n_{\mathrm{in}}^{[j]}\left(x\right) - n\left(x\right)\right) - \Gamma\left(\mathbf{n},\mathbf{C},T\right)n\left(x\right),\end{aligned} \tag{10}$$

where $g_{\mathrm{SG}} : \mathcal{E} \rightarrow \mathcal{E}$ describes change in particle type and β_{SG} the rate of change in type due to surface processes (growth/sintering), $f^{[j]}$ is the volumetric feed fraction of inlet stream j, $j \in [1, N_{\mathrm{in}}]$. The gas-phase chemistry evolves according to the set of equations for each species,

$$\frac{\mathrm{d}C_k}{\mathrm{d}t} = \dot{w}_k\left(\mathbf{C},T\right) + \dot{g}_k\left(\mathbf{n},\mathbf{C},T\right) + \frac{1}{\tau_{\mathrm{CSTR}}}\sum_{j=1}^{N_{\mathrm{in}}} f^{[j]}\left(C_{k,\mathrm{in}}^{[j]} - C_k\right) - \Gamma\left(\mathbf{n},\mathbf{C},T\right)C_k. \tag{11}$$

Here, $\dot{w}_k$ and $\dot{g}_k$ are the molar production rates of species k by gas-phase and particle reactions respectively at constant volume and $C_{k,\mathrm{in}}^{[j]}$ is the concentration in the j^{th} inflow stream. The energy balance for the system provides a description of the change in temperature, T,

$$\begin{aligned}\left(\rho_{\mathrm{g}}\overline{C}_{\mathrm{P,g}} + \rho_{\mathrm{p}}C_{\mathrm{P,p}}\right)\frac{\mathrm{d}T}{\mathrm{d}t} =& \sum_{k=1}^{N_{\mathrm{sp}}}\left[-\dot{w}_k\left(\mathbf{C},T\right)\hat{H}_k - \dot{g}_k\left(\mathbf{n},\mathbf{C},T\right)\hat{H}_k\right] - \dot{g}_{\mathrm{p}}\left(\mathbf{n},\mathbf{C},T\right)\hat{H}_{\mathrm{p}} \\ &+ \frac{1}{\tau_{\mathrm{CSTR}}}\sum_{j=1}^{N_{\mathrm{in}}} f^{[j]}\left[\sum_{k=1}^{N_{\mathrm{sp}}}\left(C_{k,\mathrm{in}}^{[j]}\hat{H}_{k,\mathrm{in}} - C_k\hat{H}_k\right) + \left(C_{\mathrm{p,in}}^{[j]}\hat{H}_{\mathrm{p,in}} - C_{\mathrm{p}}\hat{H}_{\mathrm{p}}\right)\right].\end{aligned} \tag{12}$$

Here, ρ_{g} and ρ_{p} are the gas-phase and particle molar densities respectively, $\overline{C}_{\mathrm{P,g}}$ and $C_{\mathrm{P,p}}$ are the bulk gas and the particle constant pressure heat capacities, $\hat{H}_k$ is the specific molar enthalpy of species k and N_{sp} is the number of gas-phase species. Particle processes contribute to the heat flux in the reaction terms ($\dot{g}_{\cdot}\hat{H}_{\cdot}$) and the particle flow term. Inter-phase heat transfer is assumed to be instantaneous because of the large surface area to volume ratio of small particles and the highly turbulent convective flow in typical reactor conditions – this simplification neglects radiative and conductive heat transfer to avoid modelling temperature in each particle separately. The particles are added to the thermal bulk of the system by the term $\rho_{\mathrm{p}}C_{\mathrm{P,p}}$. The effect of gas-phase molar density change is included in the expansion coefficient, Γ,

$$\Gamma\left(\mathbf{n},\mathbf{C},T\right) = \frac{1}{\rho_{\mathrm{g}}}\sum_{k=1}^{N_{\mathrm{sp}}}\left[\dot{w}_k\left(\mathbf{C},T\right)+\dot{g}_k\left(\mathbf{n},\mathbf{C},T\right)\right]+\frac{1}{\tau_{\mathrm{CSTR}}}\sum_{j=1}^{N_{\mathrm{in}}}f^{[j]}\left(\rho_{g,\mathrm{in}}^{[j]}-\rho_{\mathrm{g}}\right)+\frac{1}{T}\frac{dT}{dt}. \tag{13}$$

The PFRs are modelled as batch reactors by changing the time/distance coordinates. The mass and energy balances for a batch reactor take the same form as Eqs. (10)–(13), without the flow terms ($\tau_{\mathrm{CSTR}}^{-1}\times(\ldots)$). The thermodynamic data for rutile TiO_2 is taken from the NIST-JANAF thermochemical tables [58].

2.3.2. Reactor network configurations

The base case network has a four-CSTR dosing zone (Fig. 3, lower network), and is used to investigate the predicted final particle structure, and to study sensitivity of the particle structure to a 20 % increase/decrease in temperature of the injection streams (f_1–f_4). Subsequent studies investigate two aspects of dosing

strategy that have influenced the operation of the industrial process: injection spatial frequency and chlorine dilution. In all cases, the network parameters are chosen such that the total mass of injected reactants and reactor volume are conserved.

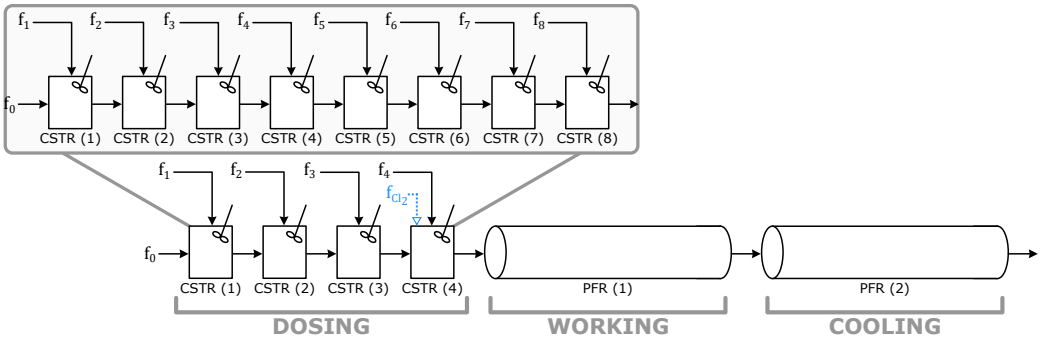

Figure 3: Alternate reactor network configurations with four/eight CSTRs with reactant injections f_1–f_4/f_8, hot oxygen flow f_0 to CSTR (1), optional chlorine dilution f_{Cl_2} to CSTR (4), and two subsequent PFRs for completion of reactions (1) and cooling (2). Chlorine dilution only studied in four-CSTR network.

The reactor network configuration is adjusted to achieve the stated research goals; however, in all studies the initial CSTR is supplied with hot O_2 gas in stream f_0 and the i^{th} CSTR is supplied with reactants in injection stream f_i (injection conditions in Table 1 and flow conditions in Table 2). Injection spatial frequency is investigated by varying the network length using: an eight-CSTR dosing zone, with CSTRs receiving half of the successive original injections (Fig. 3, upper inset, flow conditions in Table B.8); and a twelve-CSTR dosing zone, with CSTRs receiving one third of the original injections (not pictured, flow conditions given in Table B.9). Chlorine dilution is investigated for the four-CSTR configuration with chlorine injected into CSTR (4) at different flow fractions, f_{Cl_2}, and temperatures (Fig. 3, dotted arrow, conditions in Table 3).

Table 1: Stream conditions for all studies.

	Temperature (K)	$TiCl_4$ mole fraction	O_2 mole fraction
Injection f_1	600	0.26	0.74
Injection f_2–$f_{4/8/12}$	600	0.58	0.42
Hot oxygen f_0	2750	0.0	1.0

Table 2: Reactor volumetric feed fractions and residence times for 4 dosing-point study.

	Injection fraction	Main fraction	Residence time (ms)
CSTR (1)	0.42	0.58	3.0
CSTR (2)	0.25	0.75	15
CSTR (3)	0.26	0.74	15
CSTR (4)	0.23	0.77	15
PFR (1)	0.0	1.0	160
PFR (2)	0.0	1.0	1500

Table 3: Injection and chlorine flow fractions and chlorine temperatures for 4 dosing-point study.

Molar flow rate	Injection f_4	Chlorine f_{Cl_2}	Temperature (K)
2× all $TiCl_4$ added in f_4	0.19	0.20	600
2× all $TiCl_4$ added in f_1–f_3	0.15	0.33	600
1× all $TiCl_4$ added in f_1–f_3	0.21	0.11	300

3. Stochastic numerical method

The gas and particle systems are treated separately using an operator splitting approach [34] which allows solving the gas-phase kinetics (Eqs. (11)–(13)) with an ordinary differential equation (ODE) solver and evolving the particle size distributions (Eq. (10)) with a Monte Carlo method. The hybrid particle type space models are incorporated using an adapted direct simulation algorithm (DSA) [44] that handles particle choice from the combined set of particles in the particle-number list and particle ensemble, and provides machinery for performing particle processes for each type space. Simulation efficiency is enhanced using majorant kernels [59, 35], doubling [33], the linear process deferment algorithm (LPDA) [60], and a binary tree data structure [22].

3.1. Inclusion of heat release from particle processes

This work adds particle contributions to the energy balance by incorporating temperature updates during stochastic events (see Alg. Appendix A.1). This mirrors how operator splitting treats changes in concentration of the gas-phase due to particle events [34]. To do this, a discrete update is needed. A simulation particle, P_q, represents a molar concentration of

$$C\left(P_q\right) = \frac{1}{V_{\text{smp}}} \cdot \frac{1}{N_{\text{A}}} \left[\frac{(\text{particles})}{\text{m}^3} \cdot \frac{\text{mol}}{(\text{particles})}\right],$$

in the sample volume V_{smp}. For species k, the concentration change resulting from N_{event} particle events of a given type, j, is

$$\Delta C_k = \nu_k^{(j)} \left(\frac{N_{\text{event}}}{V_{\text{smp}} N_{\text{A}}}\right) \left[\frac{\text{mol}}{\text{m}^3}\right].$$

Here, $\nu_k^{(j)}$ is the stoichiometry for the k^{th} species in the j^{th} process. From Eq. (12), this triggers a discrete temperature change given by

$$\Delta T^{(j)} = -\left(\frac{1}{\rho_{\text{g}}\overline{C}_{\text{P,g}} + \rho_{\text{p}}C_{\text{P,p}}}\right)\left(\frac{N_{\text{event}}}{V_{\text{smp}}N_{\text{A}}}\right)\left(\sum_{k=1}^{N_{\text{sp}}}\nu_k^{(j)}\hat{H}_k + \nu_{\text{p}}^{(j)}\hat{H}_{\text{p}}\right)\ [\text{K}]\,, \tag{14}$$

when j is a reaction process (i.e. inception or surface growth) and

$$\Delta T^{(j)} = \left(\frac{1}{\rho_{\text{g}}\overline{C}_{\text{P,g}} + \rho_{\text{p}}C_{\text{P,p}}}\right)\left(\frac{N_{\text{event}}\nu_{\text{p}}^{\text{in}}}{N_{\text{A}}\tau_{\text{CSTR}}}\right)\left(\frac{\hat{H}_{\text{p,in}}}{V_{\text{smp}}^{\text{in}}} - \frac{\hat{H}_{\text{p}}}{V_{\text{smp}}}\right)\ [\text{K}]\,, \tag{15}$$

when j is an inflow process (note that the inflow stream may have a different sample volume, $V_{\text{smp}}^{\text{in}}$ to the reactor sample volume) and $\nu_{\text{p}}^{\text{in}}$ refers to the composition of the incoming particle. The temperature is incrementally adjusted by $\Delta T^{(j)}$ for each event of type j.

3.2. Numerical parameters

All studies use the simulation parameters in Table 4. The number of ensemble particles is chosen based on previous convergence studies for industrially representative conditions [43, 44]. Small time steps and many splitting steps are required in the reactor stages due to the strong coupling between the gas-phase kinetics and the particle growth dynamics. Larger steps are possible for modelling the cooling stage because there is no significant gas-phase coupling by this point (due to near-complete depletion of the precursor).

Table 4: Simulation parameters used in all studies.

	Value
Ensemble capacity, $N_{\max}$	2^{13}
Repeat runs, L	2^5
Particle-number threshold, N_{thresh}	10^5
Step size, Δt_{step} (s)	10^{-5}
Splitting steps per step, n_{splits}	10^2
Step size for cooling, $\Delta t_{\text{step}}^{\text{cooler}}$ (s)	10^{-4}
Splitting steps per step for cooling, $n_{\text{splits}}^{\text{cooler}}$	10^1

3.3. Performance of the particle-number/particle model

A particle-number/particle model (PN/P) was proposed to improve robustness and efficiency of the Monte Carlo simulation of particle synthesis for high rate conditions and the previous study [44] demonstrated that it is significantly cheaper to store the small particles in the particle-number model, which also reduces the risk of 'contractions' (random removals triggered when there is no space in the ensemble for inception of new particles). In the current work, we demonstrate robustness for representative industrial conditions with physically meaningful kinetics.

Robustness of the PN/P model is illustrated by considering the particle loading (number of particles stored in each sub-system model) across the reactor network. In the four CSTRs, where fresh precursor triggers rapid inception of new particles, the majority of particles in the system are small, single primaries that are stored in the particle-number model (Fig. 4, dotted lines). In fact, the total number of particles in the system, especially in CSTR (1) and CSTR (4), is frequently greater

than would be tolerated using only an ensemble pre-initialised with $N_{\max} = 2^{13}$ (Fig. 4, solid line). Thus, using a single particle model would necessitate random removals to reduce the sample volume until the numerical inception rate could be accommodated, with each removal eliminating a particle that had been resolved with computational effort.

CSTRs (1), (2) and (4) also demonstrates another advantage of the cheap storage of additional small particles – higher numerical inception rates during transient periods or temperature increase can be handled more robustly. Aggregates become more common in PFR (1), as many primaries collide and sinter. Here, the detailed particle model (Fig. 4, dashed lines) incorporates the full complexity required to describe aggregate particles fully, providing a 'best-of-both-worlds' approach. From the studies in Boje et al. [44], the greatest improvement in efficiency is achieved in the CSTR network, where primary particles can be updated and selected more efficiently using the particle-number representation.

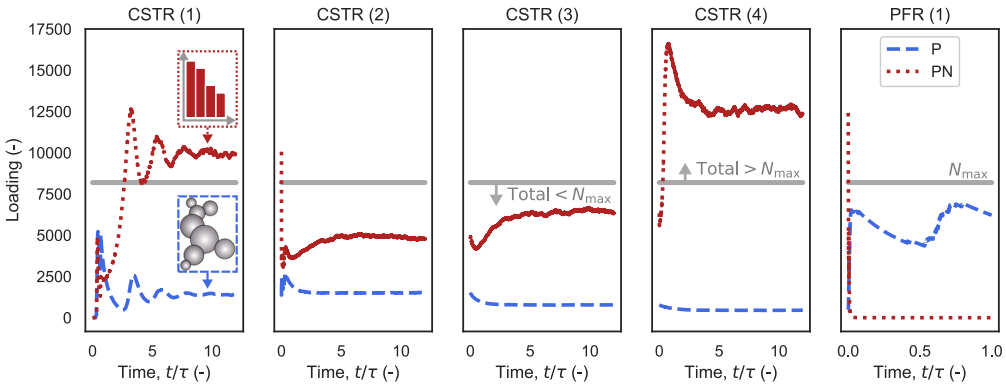

Figure 4: Number of particles stored in the particle-number list (PN) and the particle ensemble (P) in each reactor in the network. Solid line shows the ensemble maximum ($N_{\max} = 2^{13}$).

4. Process modelling results

This work aims to contribute novel understanding of industrial titania synthesis through detailed population balance modelling facilitated by enhanced robustness of the new hybrid type space approach. Understanding particle morphology is crucial because it determines the product properties and is controlled by process conditions that are challenging to study experimentally. The proposed reactor model is now used to investigate particulate properties for the base case conditions, and then to study sensitivity to different reactor parameters as outlined in Section 2.3.

4.1. Baseline assessment of particulate structure

We consider several driving questions relating to particle morphology and the outlook for controlling the synthesis process. Relevant features of particle morphology include: collision diameter, primary particle diameter, number of primary particles, and degree of sintering/neck formation. The geometric standard deviation (GSTD, σ_{g}) in primary particle diameter is used to assess typical product character,

$$\sigma_{\mathrm{g}}\left(P_q\right) = \exp\left(\sqrt{\frac{1}{n_q}\sum_{i=1}^{n_q}\left(\ln\left(\frac{d_{\mathrm{p}}\left(p_i\right)}{\overline{d}_{\mathrm{p,g}}\left(P_q\right)}\right)\right)^2}\right). \tag{16}$$

The geometric mean primary diameter, $\overline{d}_{\mathrm{p,g}}$, in Eq. (16) is computed for each particle P_q from the product of its n_q primary particle diameters,

$$\overline{d}_{\mathrm{p,g}}\left(P_q\right) = \left(\prod_{i=1}^{n_q} d_{\mathrm{p}}\left(p_i\right)\right)^{\frac{1}{n_q}}. \tag{17}$$

What is the primary particle size distribution in the aggregates?

The final aggregate particle size distribution is broad, spanning hundreds of nanometers to several microns (Fig. 5(a)), with a mean diameter of 1.85 μm. The primary particles are much smaller on average, with a mean diameter of 373 nm. This is relatively large compared to the targeted industrial range of around 200 nm–300 nm given by Park and Park [2]; however, it is within the bounds of other hot wall and flame studies they list with similar temperatures and residence times. Some discrepancy is to be expected in the current study. The idealised reactor model [43] assumes perfect mixing in the dosing zone, eliminating mixing and heat transfer limitations. Since inception requires decomposition of the precursor while surface growth consumes it directly, particle growth might occur more rapidly when reactants combine instantaneously, yielding larger particle diameters compared to the operational range. The model is also not directly calibrated to reproduce this experimental data and it is possible that improved correspondence between the simulated and observed particle morphology could be obtained in this manner (however, this data is not currently accessible). The primary particles in the cooled outflow are significantly polydisperse, with a geometric standard deviation in diameter of 1.6.

What is the aggregate composition?

Cooled aggregates consist of 22 connected primary particles (Fig. 5(b)) on average, although free primary particles and many larger aggregates containing 50–150 primaries also exist. Some free primary particles (see dotted line in Fig. 5(a)) have sizes significantly above the desired range; however, in general aggregate size increases with the number of constituent particles and the marginal distributions of both primary particles and aggregates have long tails.

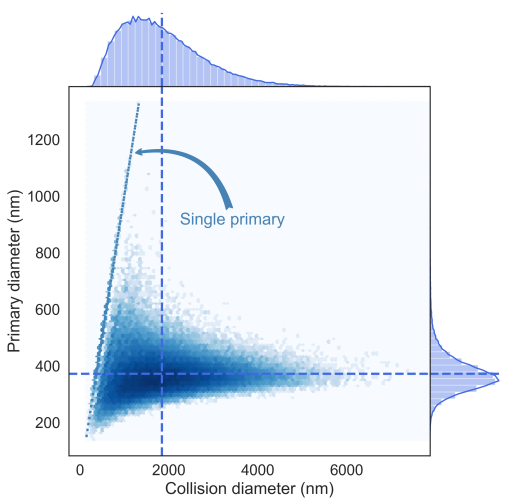

(a) Aggregate and primary sizes

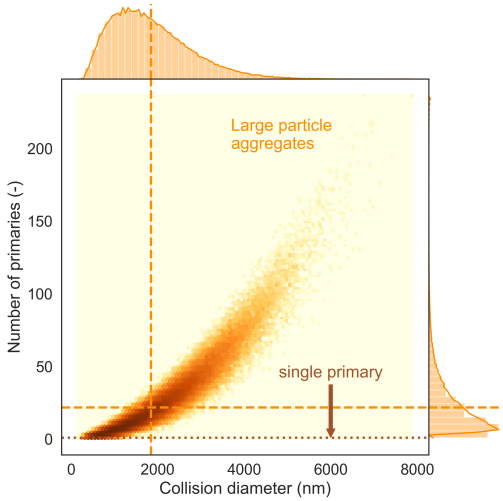

(b) Aggregate size and composition

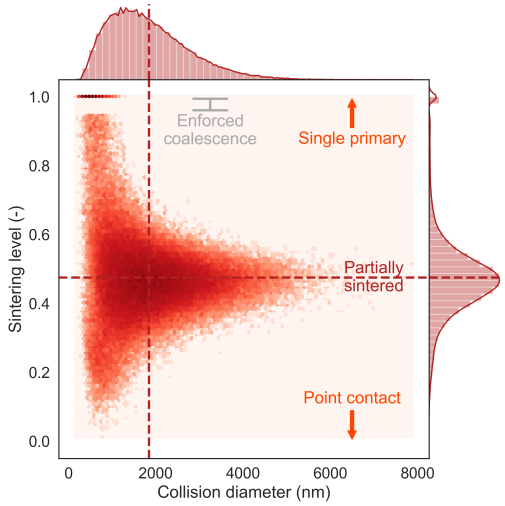

(c) Aggregate size and cohesion

Figure 5: Joint property distributions with marginal kernel density estimates (bandwidths: 0.01) and histograms for the cooled particles. Dashed lines indicate property mean values and dotted line indicates single primaries.

How strongly connected are the primary particles?

When two particles coagulate, the resulting particle initially has point contact where the collision occurred. When the neighbouring particles sinter or undergo surface growth at temperatures relevant to this study, the area of their connection increases, rendering an aggregate that is increasingly difficult to break down by mechanical force. There is limited aggregate sintering in the dosing zone, where the sintering levels range between 0 (point contact) and 1 (fully sintered/free primary). Neck growth occurs to a larger extent in the PFRs, where there is also less inception of free primaries, and this yields a more compact sintering level distribution with most particles somewhat sintered. The average sintering level of the cooled product is 0.48, i.e. the final particulate product consists of strongly bonded primaries (Fig. 5(c) – the absence of simulation particles with sintering levels in the band 0.95–1.0 is an artefact of the model that enforces coalescence for particles with $s_{ij} > 0.95$).

The cumulative distributions of primary and neck diameters (Fig. 6) demonstrate the high level of sintering more quantitatively for the cooled product. Approximately 75 % of the population has primary particle diameters in the range 100 nm–400 nm (indicated with solid lines in Fig. 6) while around 20 % of the neck diameters exceed 100 nm. The neck diameter has severe implications for the ease of separation of particles to achieve a desired size – crystals with significant necks may not be easily split into smaller primary particles, whereas small necks are easy to break with post-process milling. Models for milling of aggregate particles could be used to further inform process understanding and such models could also consider other factors such as the distance of a primary pair from the centre of mass of the particle to determine fragmentation efficiency [41].

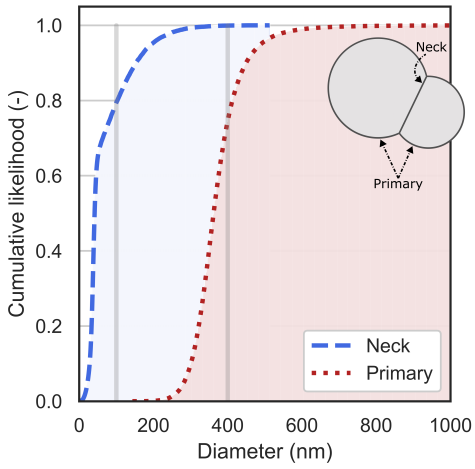

Figure 6: Cumulative distribution of cooled particle primary and neck diameters with 100 nm–400 nm range indicated as solid vertical lines.

4.2. Sensitivity to process conditions and configuration

Ideally, a model for the industrial process should inform optimal process design, including operating conditions and strategies to enhance product quality and minimise cost of post-processing steps such as milling. The questions that follow illustrate the degree of process/model sensitivity to such design choices.

The commercial titania reactor is operated at very high conversion such that the reactions go to completion. The yield is expected to be relatively insensitive to conditions such as temperature within a realistic range. In all cases presented in this paper, the reactions are complete before the end of the reactor. However, because the morphology of the particles is critical to the end-product quality, reactor yield cannot be used in isolation to judge the merits of different options. For example, if additional $TiCl_4$ is used in the surface reaction, the resulting primary particles might be too large relative to the desired range. This suggests that

achieving a higher yield does not necessarily improve the reactor performance.

What is the effect of injection temperature?

Reactor temperature is an important parameter: decomposition of the $TiCl_4$ is endothermic, so energy is required to initiate the process. With the exothermic oxidation step, there is a risk of thermal runaway or hotspot development, which would negatively affect product quality. The reactant injections offer one means to control temperature. The baseline injection temperature of 600 K is in the scope of what could be used in the industrial process. The temperature range of 480 K–720 K chosen for this study is fairly broad and is not likely to be plausible in the real process. These values were selected as the upper and lower test points to provide an idea of the possible influence exerted by this process parameter and asses the extent to which it is important for determining particle structure.

The outlet temperature from PFR (1) shows unsurprising correlation with increasing or decreasing reactant injection temperature (Table 5), but only a moderate change was observed in this study (increasing the temperature of the reactant stream reduces the thermal cooling it can provide to the exothermic oxidation process); however, the reaction goes to completion in all three cases. The hottest injection did not produce a 'hot spot' or runaway temperature increase in the reactor.

Table 5: Effect of injection temperature on reactor outlet temperature.

Injection temperature (K)	PFR (1) outlet temperature (K)
480	1540
600	1630
720	1700

Effects of temperature on the particles are more difficult to analyse due to the complex nature of interdependent processes that occur in the multi-injection system, with all particle processes accelerated by increasing temperature. The collision diameter distributions in the CSTR network are slightly bimodal, with a small peak near the incepting particle size (0.49 nm) and a larger peak in the 100 nm–1000 nm range. These peaks change with temperature: the hotter system induced by a higher injection temperature (Fig. 7, dotted line) has the largest inception mode, lower reactant concentration driving lower surface growth and higher sintering, in the hotter system (cf. Fig. 7, dashed line).

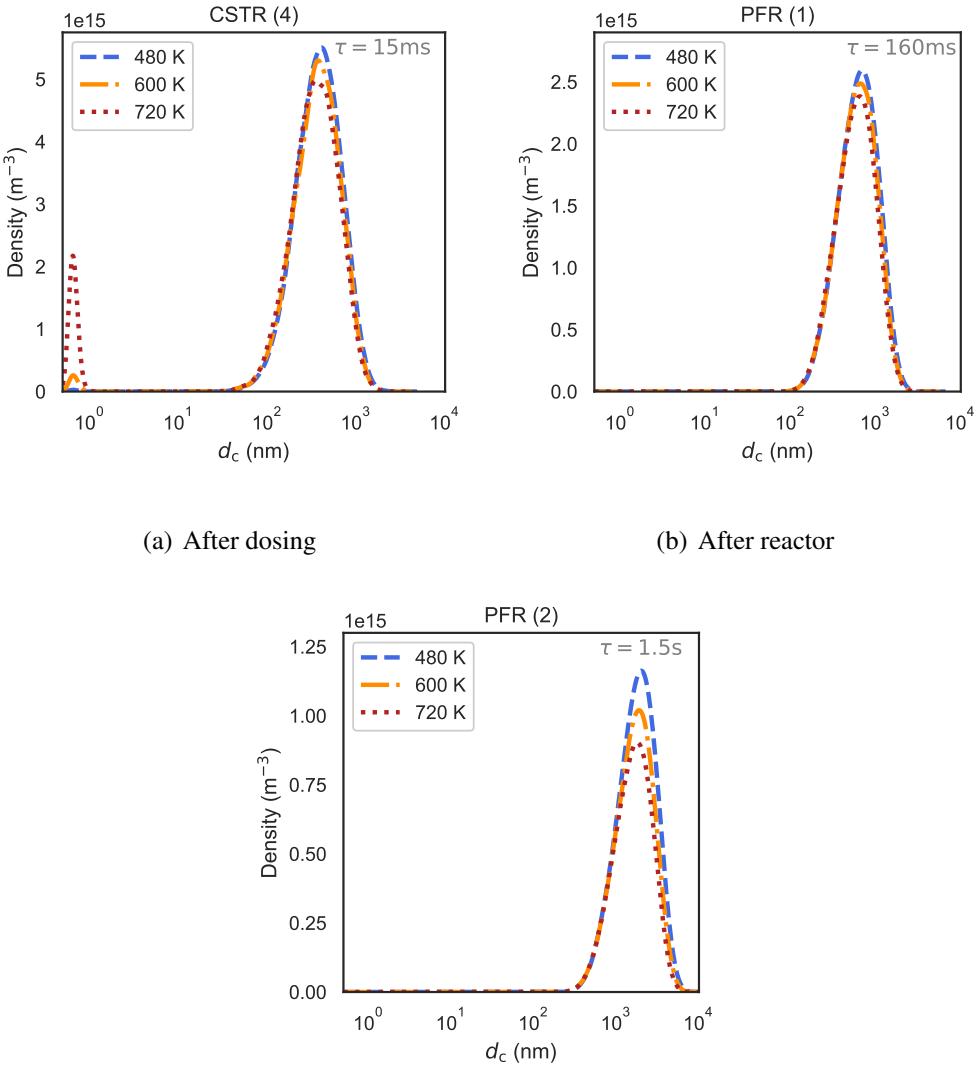

(a) After dosing

(b) After reactor

(c) After cooling

Figure 7: Scaled kernel density estimates (bandwidth: 0.1) of collision diameter distributions in the reactor network with different injection temperatures (note vertical axis limits differ to resolve different number densities in the three reactors).

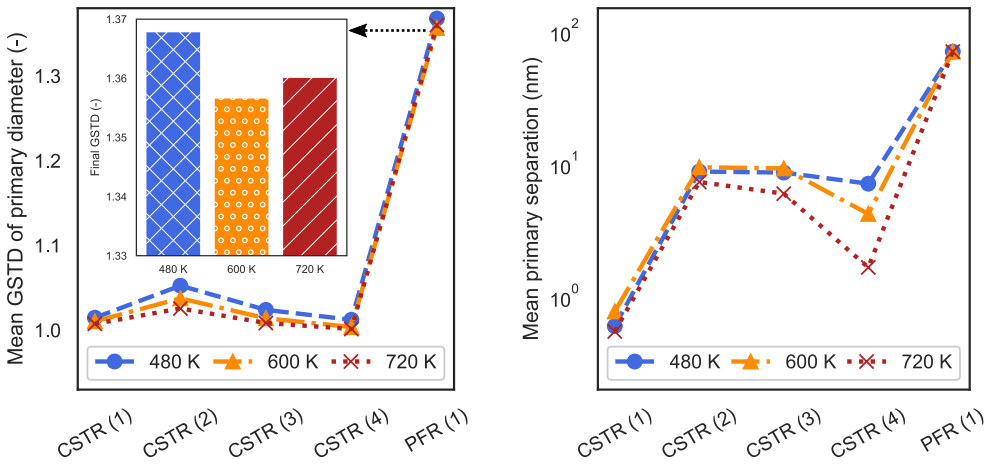

(a) GSTD

(b) Separation

Figure 8: Mean GSTD of primary diameter and mean primary particle separation across the reactor network with different injection temperatures.

Downstream, in PFR (1), there is little/no evidence of an inception peak and the distributions are similar due to coagulation. The number density decreases along the network due to coagulation, and the main difference in distributions is a reduction in number density with increasing temperature. Assessment of the mean geometric standard deviation in primary size (Fig. 8(a)) across the network shows a similar homogenization in PFR (1). The higher temperature systems seem to produce less disparate primaries throughout all stages and this could help to yield a more consistent product; however, the final GSTD shows no clear influence of temperature. The increase in GSTD between the CSTR network, which models the dosing zone, and the end of PFR (1), which models the working zone, can be attributed to additional surface growth and high-temperature sintering-to-coalescence in the final reactor zone, which has an order of magnitude longer res-

idence time. The predicted yield is essentially unchanged across the temperature range studied here, so the reduced peak with increasing temperature in PFR (2) is not due to reduced product formation. There are several possible contributing factors. Particle number density is reduced by coagulation, which occurs to a greater extent at higher temperatures. Additionally, this study employed a fixed amount of heat removal in the cooler – thus the higher temperature cases have higher final temperatures than the low temperature case which modifies the flow conditions.

The overlapping spheres particle model allows additional insight beyond comparing particle size distributions. The size distribution of the necks between connected primaries can also be assessed (Fig. 9) and this highlights several interesting features of the relationship between temperature and particle structure: (i) there are more particle inceptions at higher temperatures, lowering the average neck size in the CSTR network (free primaries have no necks and small particles coalesce rapidly); (ii) a bimodal neck distribution develops in PFR (1) where most of the remaining free primary particles coagulate (cf. loss of the small peak between Fig. 7(a) and Fig. 7(b)), with a large peak for necks less than 100 nm in radius and a smaller peak for necks above this size; and (iii) the higher temperatures increase the sintering rate, yielding a larger mean size for the small-radius mode without significant change in the large-radius mode.

Comparison of the separation between connected primaries also highlights different sintering behaviour: primaries are closer together in the hotter (720 K) study (Fig. 8(b)). Insights about particle cohesion could be used to choose process conditions that result in lower post-processing requirements to separate primaries to achieve suitable pigment sizes.

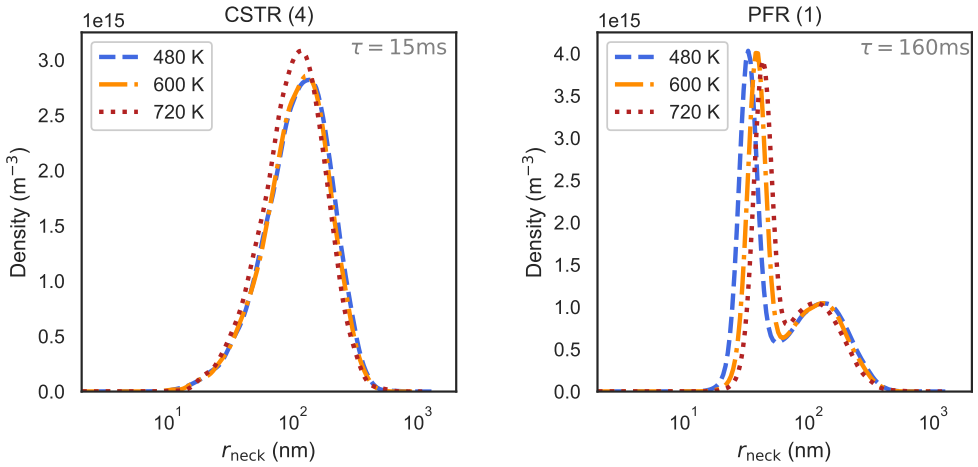

(a) After dosing

(b) After reactor

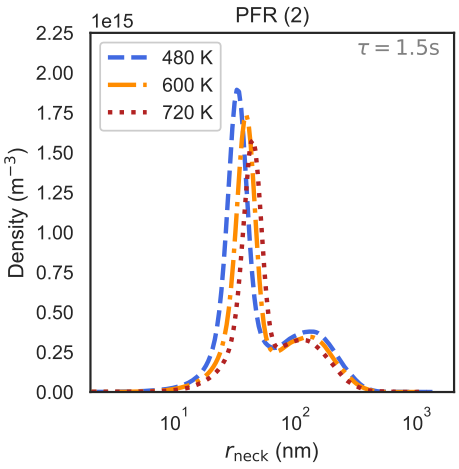

(c) After cooling

Figure 9: Scaled kernel density estimates (bandwidth: 0.1) of neck radius distributions in the reactor network with different injection temperatures (note vertical axis limits differ to resolve different number densities in the three reactors). Free primaries ("$r_{\text{neck}} = 0\,\text{nm}$")) not represented on the log scale.

How do dosing strategies alter particle size and polydispersity?

The dosing scheme is modified by increasing the number of CSTRs (each with a fresh reactant feed) to achieve smaller, more frequent injections (cf. Fig. 3, upper/lower networks). This reduces the range of geometric standard deviations in primary diameters in the aggregates and, to a lesser extent, produces smaller primary particles on average (Fig. 10). These findings indicate that increasing the spatial frequency of reactant injections produces a higher quality, more consistent product which is in keeping with observation of the multi-injection, industrial process.

To study the differences further, five particles are extracted for each configuration using a data clustering 'k-mediod' algorithm [61] from the *pyclustering* python library [62] based on the property sets, Σ_q:

$$\Sigma_q = \left\{ d_{\mathrm{c}}\left(P_q\right), \overline{d}_{\mathrm{p}}\left(P_q\right), n_q\left(P_q\right), \overline{s}\left(P_q\right) \right\}.$$

Σ_q thus accounts for the aggregate collision diameter, average primary diameter, number of primaries and average sintering level – the properties used to assess particle structure for the base case conditions. The five clusters group the particle system according to principal observations of these characteristics. Increasing the frequency of injections reduces the range of primary particle sizes, producing mediods with more similar primary size properties and eliminating the large diameter centre, cluster 5, observed for the four-injection configuration (Fig. 11(a)). The five clusters have disparate primary counts in all cases (Fig. 11(b)), with clusters 1–3 containing fewer than ten primaries and clusters 4–5 including particles with more than ten primaries. The twelve-injection configuration has the largest upper bound on primary count.

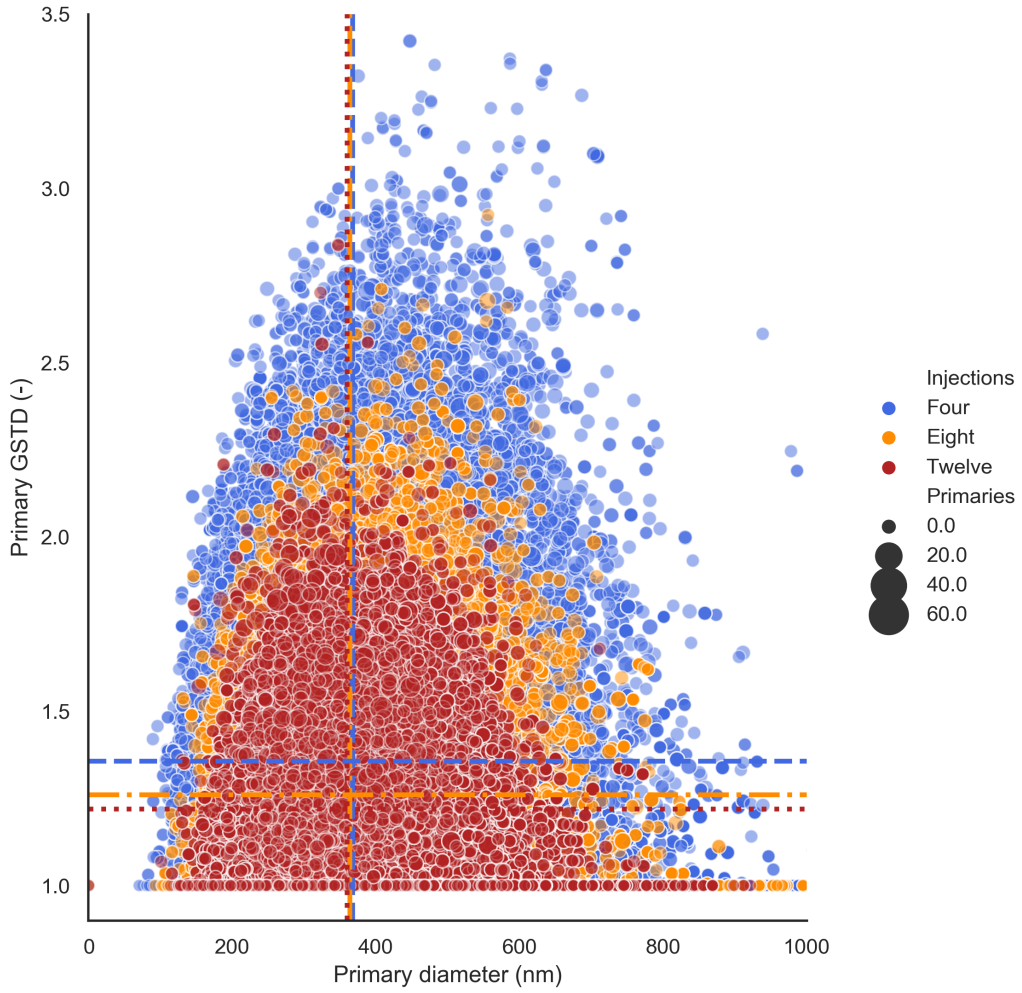

Figure 10: Mean and geometric standard deviation (GSTD) of primary diameters in each aggregate for different reactant dosing frequencies at the end of the reactor (i.e. after PFR (1)). The marker sizes reflect the relative number of primaries in the aggregate. The dashed lines indicate the mean values for the sample.

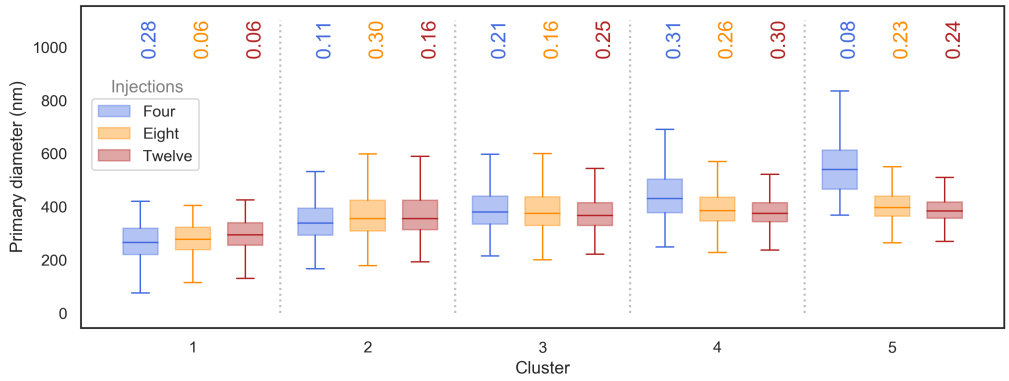

(a) Primary diameter clusters

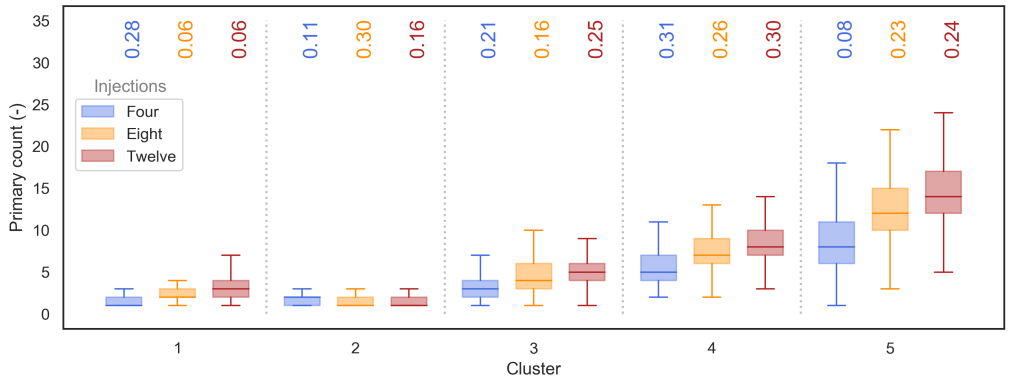

(b) Primary count clusters

Figure 11: Comparison of 5 particle centres selected using k-mediod clustering. The numbers above the boxes indicate the portion of the total sample in the cluster.

Does chlorine dilution affect particle size and structure?

Synthesis of titania from $TiCl_4$ produces chlorine as a by-product. The chlorine can be recycled to the chlorination stage that produces $TiCl_4$ or cooled and re-injected into the reactor [63, 4] to reduce temperature, dilute the system or inhibit the surface oxidation process, all of which target reduced particle size.

Three chlorine dilution strategies are assessed (Table 3): adding 20 % by volume at 600 K, adding 33 % by volume at 600 K and adding 11 % by volume at 300 K. These cases assess some extremes on possible chlorine strategies: dilution at the injection temperature vs ambient temperature; dilution with double the injection flow rate vs with the maximum chlorine produced up to this point.

The developed PSDs are altered in all three new schemes (Fig. 12). The injection of chlorine produces a larger peak around the inception size in CSTR (4) (see dashed/dotted lines cf. original in solid grey). In contrast to the base case, this is still present after PFR (1) in all chlorine cases. The small-particle peak vanishes by the end of the cooling stage due to coagulation; however, there is still discrepancy in the final distributions with a smaller mean particle size, lower standard deviation and reduced range (Table 6).

Table 6: Effect of chlorine dosing on final particle collision diameter distributions: range, arithmetic mean and standard deviation (STD), with ratios computed using respective base case value as the denominator to demonstrate relative effect.

Case	Range (nm)	Mean (nm)	STD (nm)	Mean ratio	STD ratio
0 % Cl_2 base case	7710	1850	913	1.00	1.00
20 % Cl_2 at 600 K	6830	1750	876	0.948	0.959
33 % Cl_2 at 600 K	6351	1550	784	0.841	0.858
11 % Cl_2 at 300 K	7040	1640	818	0.891	0.896

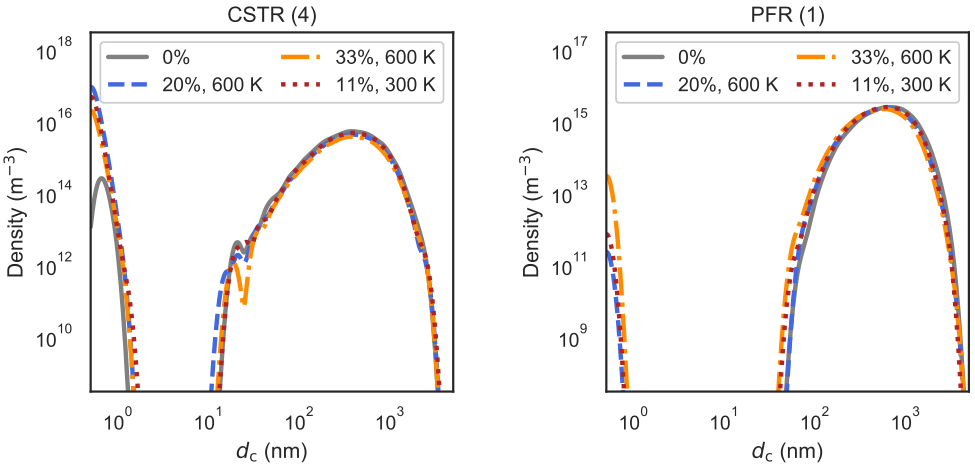

(a) After dosing

(b) After reactor

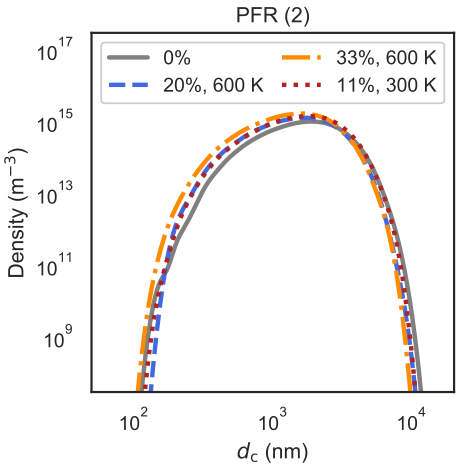

(c) After cooling

Figure 12: Kernel density estimates (bandwidths: 0.1) of collision diameter distributions immediately after CSTR (4) (where chlorine is injected), after PFR (1) and after PFR (2) with solid line showing 0 % addition for comparison (note axis limits differ).

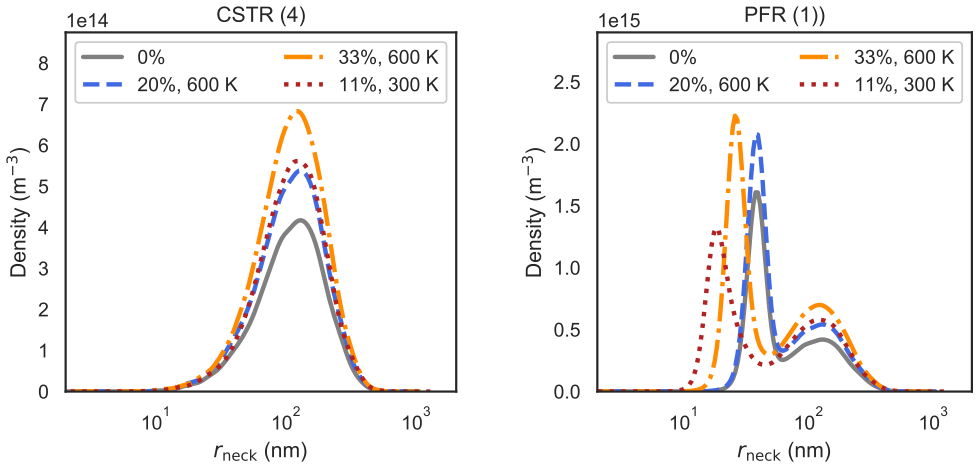

(a) After dosing

(b) After reactor

(c) After cooling

Figure 13: Scaled kernel density estimates (bandwidth: 0.1) of neck radius distributions in the reactor network with different chlorine injections (note vertical axis limits differ to resolve different number densities in the three reactors). Free primaries ("$r_{neck} = 0$ nm")) not represented on the log scale.

The mean primary particle size is also reduced in all cases, although the difference is smaller. Dosing with chlorine also shifts the particle neck distributions (Fig. 13), producing a larger density of small necks (600 K injections) or reducing the mean size of the small necks (large injections at both temperatures). Thus injection of chlorine could be an effective strategy to control particle size and polydispersity. The most significant reduction in mean and polydispersity is observed for the case with 33 % Cl_2 at 600 K – this suggests that cooling the separated chlorine to room temperature for this purpose is less useful than increasing the chlorine flow rate.

4.3. Characterisation of fractal structure

The fractal-like nature of aerosol particles can be characterised by relating the primary and aggregate diameters with the number of primary particles in the aggregate,

$$n_q\left(P_q\right) = k_\mathrm{f}\left(\frac{d_\mathrm{g}\left(P_q\right)}{\overline{d}_\mathrm{p}\left(P_q\right)}\right)^{D_\mathrm{f}}. \tag{18}$$

D_f is the fractal dimension, k_f is the fractal pre-factor and $d_\mathrm{g}\left(P_q\right)$ is the radius of gyration of particle P_q (Eq. (7)). The fractal dimension is often used to classify particle structure, with a fractal dimension of 3.0 corresponding to a spherical particle and lower fractal dimensions indicating more open, linear particle shapes. Fractal dimensions can be defined by simulating coagulation for populations of coagulating monodisperse (uniform properties) and polydisperse (distribution of properties) primary particles [64].

For monodisperse primary particles BCCA should produce a fractal dimension of 1.9. Polydispersity has been shown to alter fractal structure [65]. Eggers-

548 dorfer and Pratsinis [64] found that, for a BCCA coagulation model, increasing
549 primary particle polydispersity (as measured by the GSTD) produces decreasing
550 fractal parameters in the GSTD range 1.0–2.0, with approximate corresponding
551 parameter values in the ranges 1.4–1.1 for k_f and 1.9–1.7 for D_f. The fractal struc-
552 ture of particles has been shown to be a strong function of the particle growth
553 processes. Schmid et al. [66] found significant dependence on the relationship
554 between the coagulation and sintering processes and Eggersdorfer et al. [65] note
555 that sintering tends to increase the fractal dimension (particle aggregates more
556 compact/spherical) whilst polydispersity decreases the fractal dimension (particle
557 aggregates more open). Aerosol particles typically have a fractal dimension in the
558 range 1.6–2.5 [65]. Elucidating the fractal structure relationship is important be-
559 cause it provides information about the particle geometry, which governs product
560 properties such as light scattering propensity but also determines local chemical
561 activity and heat transfer properties [65].

562 The polydispersity is classified using the geometric standard deviation in pri-
563 mary particle diameters. In other work, this has parametrized the lognormal dis-
564 tribution of primary particles used as a starting point in simulations to determine
565 fractal dimension. The advantage of the current work is that it provides suffi-
566 cient detail in the particle model to estimate the fractal structure of particles that
567 have polydispersity arising from real processes (e.g. sintering, surface reaction) in
568 the industrial reactor. The fractal structures created in the different test cases pre-
569 sented in this work were characterised by fitting (Fig. 14) the simulation data using
570 Eq. (18). In general, the relationship observed by Eggersdorfer and Pratsinis [64]
571 was found to hold (Table 7) for fractal dimension, with lower D_f values predicted
572 for the cases with higher polydispersity. The prefactor values are higher than re-

ported in the previous study. However, the prefactors and fractal dimensions are sensitive to the minimum primary particle count cut-off used in the fitting, with larger values of D_f and smaller values of k_f resulting from exclusion of aggregates with only a few primaries. There is a trade-off in prediction uncertainty as points are excluded in this cut-off (Fig. 14, density histogram). The fractal fit provides a reasonable description of the full set of aggregates, in spite of weaker agreement at the edges of the spectrum due to low number density of particles with the largest primary counts and reduced applicability of fractal models to particles with few primaries.

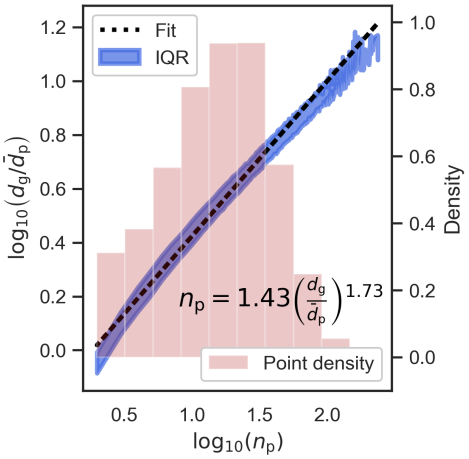

Figure 14: Fitted fractal relationship (dashed line) between the logarithms of number of primary particles per particle and particle-to-primary diameter ratio for the base case simulation data. The interquartile range (IQR, i.e. middle 50 %) is indicated by the filled area and the fitted slope and intercept parameters are shown in context as the exponent and prefactor of the equation in the lower right. The histogram indicates density of data for different aggregate sizes.

Table 7: Fitted fractal parameters and mean geometric standard deviation (GSTD) in primary diameters from simulation data.

Case	Fractal dimension	Fractal pre-factor	GSTD
	D_f	k_f	σ_g
600 K, 4 injections	1.7	1.4	1.6
480 K, 4 injections	1.7	1.4	1.6
720 K, 4 injections	1.7	1.4	1.6
600 K, 8 injections	1.8	1.5	1.4
600 K, 12 injections	1.8	1.5	1.4

It is useful to relate the simulated particle properties to a well-known, mean structural property because this provides a simple method of assessing how process conditions affect particle geometry – a relationship that can be challenging to investigate experimentally. However, it should be noted that the BCCA model used here applies best to particle coagulating in the free-molecular, rather than the transition, regime. For larger particles, a diffusion-limited cluster-cluster model would be more appropriate. Lindberg et al. [23] reported that no appreciable difference was observed when testing these two coagulation models in hot wall reactor simulations. There is further a relatively narrow gap between the fractal dimensions predicted by ballistic and diffusion-limited aggregation. Thus, this caveat is not expected to undermine the utility of the current study assessing the trend in geometries predicted for different process design choices.

4.4. Comparison of simulated and real particle images

The model data can be used to simulate scanning electron microscopy (SEM) images, providing a view of the developed particles that is directly comparable

with images of real particles coming out of a titania reactor. Comparison of a real particle image (Fig. 15) with the simulated images (Fig. 16) shows qualitatively similar properties such as highly non-spherical aggregate structures comprised of many smaller, partially sintered primary particles; however, these images also highlight the many relatively large primary particles produced in the simulations, especially for the non-diluted case (Fig. 16(a)).

This observation supports the preceding comments on size ranges compared to those reported for the industrial process. The simulations undertaken in this study employed industrially representative conditions, but are not a perfect match for the exact conditions used to generate the real particles from which the image is created. There is uncertainty in the numerical rates used – associated with generation of constants from first-principles calculations and by fitting to data from less severe process conditions – which is amplified by the high rates and fast dynamics of this process. Images with and without chlorine dilution (Fig. 16(a) cf. Fig. 16(b)–16(d)) do, however, illustrate effectiveness of injecting cool chlorine in reducing particle/aggregate size by cooling and diluting the system – which is likely closer to the industrial operation in any case. These simulated SEM images highlight the utility of the detailed particle model in providing morphological information about the particles for visualisation.

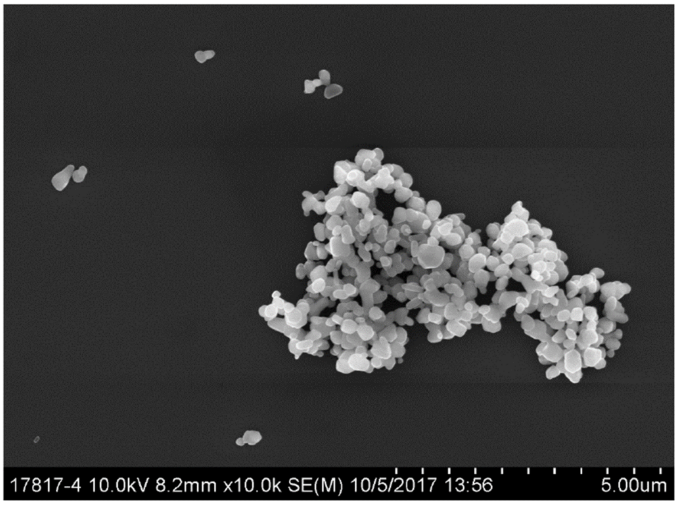

Figure 15: Real particle SEM (image courtesy of, and with permission from, Venator).

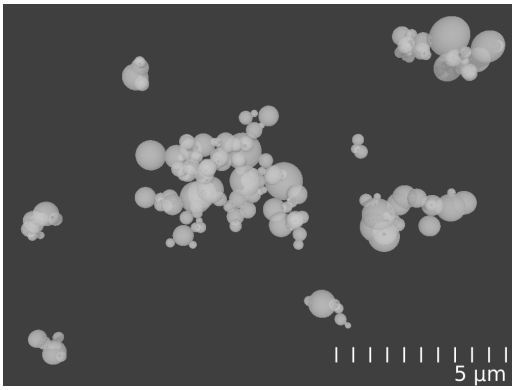

(a) 0 % Cl_2 base case

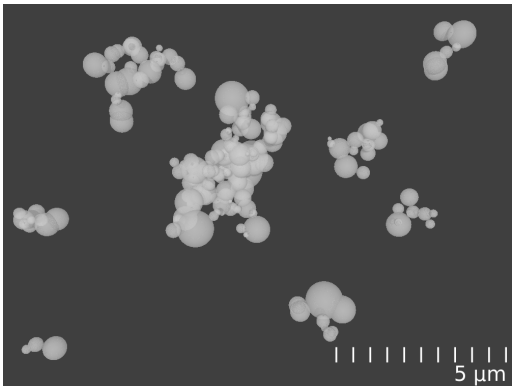

(b) 20 % Cl_2 at 600 K

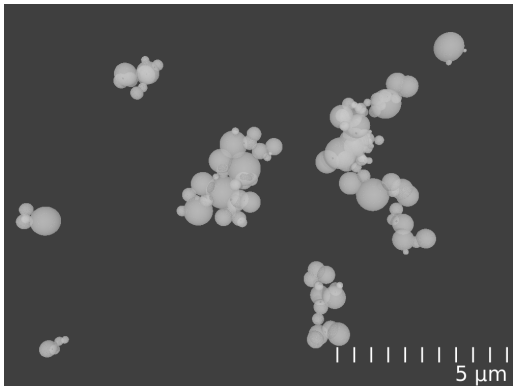

(c) 33 % Cl_2 at 600 K

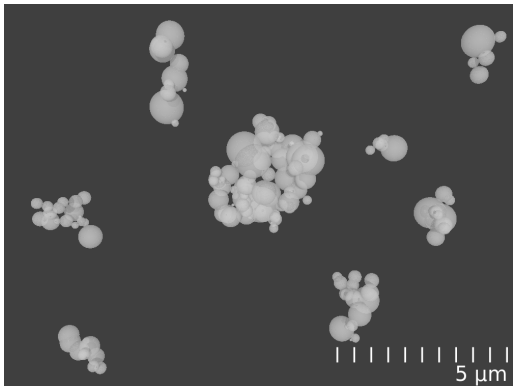

(d) 11 % Cl_2 at 300 K

Figure 16: Simulated SEMs for cooled particle product.

5. Conclusion

This work has used the recently proposed particle-number/particle algorithm to aid detailed simulation of titania synthesis under industrially-relevant conditions. Robustness and efficiency of this algorithm enable the study of rapid particle inception and growth using a complex type space model, even in the presence of exotherms and transience. The overlapping-spheres particle model was used to provide insight into the development of complex aggregate structures in the industrial synthesis of pigmentary titania. The final particle population exhibits broad aggregate size distributions, with a range of sintering levels (necks) and primary numbers, and this has implications for ease of post-processing to achieve a desired product specification. The average primary particle size is slightly above the desired size of approximately 300 nm and it is noted that this could be due to simplification of the flow field which produces idealised mixing. There may further be discrepancy in how particle size is measured in industry compared to in the model. The neck radius and degree of primary separation were studied in addition to properties of the particle size distribution, and it was shown that changing reactant dosing temperature alters particle attachment characteristics that are important for post-processing efficiency.

Reactant dosing strategy is also important – with more frequent dosage creating a narrower range of particle properties. Of course, in practice there may be reactor design limitations on the number of feasible injection points and the studies shown here should be supported by insights from computational fluid dynamics studies of mixing behaviour. Of course, in practice there may be reactor design limitations on the number of feasible injection points and the studies shown here should ideally be supported by insights from computational fluid dynamics studies

of mixing behaviour. It is computationally infeasible to combine fluid dynamics simulations with the detailed chemistry and particle model used in this work. Mixing has been studied independently in several cases [67, 68]; however, flow-only or simplified-kinetics CFD studies are ill-suited to elucidating the flow behaviour of this system because of extensive coupling between the gas phase chemistry, the energy balance and the particle system. Simplifying the description of particles will introduce its own approximations, for example the method of moments is typically combined with CFD but performs poorly for bimodal distributions. In other recent work [19], CFD simulations with chemistry and a simplified particle model have been post-processed using a detailed particle model to obtain more resolution in the particle type space. This approach is already challenging and is unlikely to be sufficient to describe the interactions between the particles and the flow with industrially relevant particle loadings. A different strategy would be to use radioactive tracer studies to investigate the residence time distribution in the commercial reactor itself. However, the modelling approach is relatively attractive because it is non-invasive. In general, the reduction in particle size and geometric deviation for increasing injection points agrees with industrial practice where multiple injection points are employed. Chlorine dosage was also shown to reduce the average size, standard deviation and range of the distribution of particles, providing another option for achieving desired sizes in the industrial process. Comparison of simulated images with an SEM image from a titania plant provides a useful qualitative assessment of model predictive capacity. Simulated imaging also allows investigation of morphology developed under different conditions.

Acknowledgements

This project is partly funded by the National Research Foundation (NRF), Prime Minister's Office, Singapore under its Campus for Research Excellence and Technological Enterprise (CREATE) programme. The authors would also like to thank Venator for financial support.

Nomenclature

Upper-case Roman

A	Surface area	$[\mathrm{m}^2]$
C	Concentration	$[\mathrm{mol\,m}^{-3}]$
$\mathbf{C}$	Connectivity matrix	
C_P	Constant pressure heat capacity	$[\mathrm{J\,K}^{-1}\,\mathrm{mol}^{-1}]$
D_f	Fractal dimension	
$\hat{H}$	Specific molar enthalpy	$[\mathrm{J\,mol}^{-1}]$
I	Inception rate	$[\mathrm{mol\,m}^{-3}\,\mathrm{s}^{-1}]$
K	Coagulation kernel	$[\mathrm{m}^{-3}\,\mathrm{s}^{-1}]$
L	Number of repeat runs	
M	Number of time steps	
M_0	0^{th} number moment	$[\mathrm{m}^{-3}]$
MW	Molecular weight	[g mol]
N	Number	
N_A	Avogadro's constant	$[\mathrm{mol}^{-1}]$
P	Particle	
R	Rate	[process specific]
T	Temperature	[K]
V	Volume	$[\mathrm{m}^3]$

Lower-case Roman

d	Diameter	[nm]
d_{ij}	Centre-to-centre distance of primary particles i and j	[nm]
f	Volumetric feed fraction	
g	Surface growth type-change function	
$\dot{g}$	Molar rate due to particle process	[mol m^{-3}]
k_f	Fractal prefactor	
m	Mass	[kg]
n	Particle number concentration	[m^{-3}]
n_q	Primary count for particle P_q	
p	Primary particle	
r	Radius	[nm]
s	Sintering level	
t	Time	[s]
$\dot{w}$	Molar rate due to particle process	[mol m^{-3}]
x	Particle type variable	
x_{ij}	Centre-to-neck distance from primary particle i to j	
y	Particle type variable	
z	Particle system	
$\mathbf{z}$	Primary centre of mass coordinates	[nm]

Upper-case Greek

Γ	Gas-phase expansion coefficient	
Σ	Property set	

Lower-case Greek

β	Surface growth rate	$[\mathrm{m^2\,m^{-3}\,s^{-1}}]$
η	Number of components	
ν	Stoichiometry	
π	Pi (constant)	
ρ	Mass/molar density	$[\mathrm{kg\,m^{-3}/mol\,m^{-3}}]$
σ	Standard deviation	
τ	Residence time	[s]

672

Subscripts

add	Added
c	Collision
coag	Coagulation
g	geometric
i	Index variable
in	inflow
j	Index variable
k	Index variable
max	Maximum

out	Outflow
p	Primary particle
q	Index variable
SG	Surface growth
smp	Sample
sp	Species
split	Splitting time
thresh	Threshold

Symbols

$\mathcal{E}$	Generic particle type space
$\mathcal{M}$	Small particle type space
$\mathcal{X}$	Large particle type space

Abbreviations

BCCA	Ballistic cluster-cluster algorithm
CSTR	Continuous stirred tank reactor
DSA	Direct simulation algorithm
(G)STD	(Geometric) standard deviation
IQR	Interquartile range
LPDA	Linear process deferment algorithm
ODE	Ordinary differential equation

PBE Population balance equation

PFR Plug flow reactor

PN/P Particle-number/particle

PSD Particle size distribution

SEM Scanning electron microscopy

Appendix A. Algorithms

Algorithm Appendix A.1: Simplified Strang operator-splitting scheme with heat release due to particulate processes added in the particle solver step (***emphasised in bold italics***).

Input: State $((\mathbf{C}_0, T_0, \Gamma_0), (z_{\mathcal{M},0}, z_{\mathcal{X},0}))$[a], sample volume $V_{\text{smp},0}$, time t_0, final time t_f

Output: State $\left(\left(\mathbf{C}_f, T_f, \Gamma_f\right), \left(z_{\mathcal{M},f}, z_{\mathcal{X},f}\right)\right)$, sample volume $V_{\text{smp},f}$

Set $t \leftarrow t_0$, $\Delta t \leftarrow \left(t_f - t_0\right)$, $(\mathbf{C}, T, \Gamma) \leftarrow (\mathbf{C}_0, T_0, \Gamma_0)$, $(z_{\mathcal{M}}, z_{\mathcal{X}}) \leftarrow (z_{\mathcal{M},0}, z_{\mathcal{X},0})$, $V_{\text{smp}} \leftarrow V_{\text{smp},0}$.

while $t < t_f$ **do**

- Solve gas-phase chemistry for $\left[t, t + \frac{\Delta t}{2}\right] \rightarrow$ update $(\mathbf{C}, T, \Gamma)$.
- Set $t_{\text{process}} \leftarrow t$.
- Scale sample volume for gas-phase expansion Γ.
- Compute total process rate $R\left(z_{\mathcal{M}}, z_{\mathcal{X}}\right)$.
- **while** $t_{process} < t + \Delta t$ **do**
  - Choose update time $\tau \sim \exp\left(R\right)$.
  - **if** $t_{process} + \tau < t + \Delta t$ **then**
    - Choose and perform a particle process $\rightarrow$ update $(z_{\mathcal{M}}, z_{\mathcal{X}})$.
    - ***Compute changes to gas-phase*** $\rightarrow$ ***update*** $(\mathbf{C}, T, \Gamma)$***.***
    - ***Scale sample volume for gas-phase expansion*** Γ***.***
    - Increment $t_{\text{process}} \leftarrow t_{\text{process}} + \tau$.
  - **end**
- **end**
- Set $t \leftarrow t_{\text{process}}$.
- Solve gas-phase chemistry for $\left[t + \frac{\Delta t}{2}, t + \Delta t\right] \rightarrow (\mathbf{C}, T, \Gamma)$.
- Scale sample volume for gas-phase expansion Γ.
- Increment $t \leftarrow t + \Delta t$.

end

[a] Components $z_{\mathcal{M}}$ and $z_{\mathcal{X}}$ refer to the particle systems for the type spaces $\mathcal{M}$ (the particle-number model) and $\mathcal{X}$ (the detailed particle model) respectively. This notation was introduced in Boje et al. [44].

Appendix B. Tables

Table B.8: Reactor volumetric feed fractions and residence times for 8 dosing-point study.

	Injection fraction	Main fraction	Residence time (ms)
CSTR (1)	0.26	0.74	1.9
CSTR (2)	0.21	0.79	1.5
CSTR (3)	0.15	0.85	8.6
CSTR (4)	0.13	0.87	7.5
CSTR (5)	0.15	0.85	8.6
CSTR (6)	0.13	0.87	7.5
CSTR (7)	0.13	0.87	8.6
CSTR (8)	0.12	0.88	7.5

Table B.9: Reactor volumetric feed fractions and residence times for 12 dosing-point study.

	Injection fraction	Main fraction	Residence time (ms)
CSTR (1)	0.19	0.81	1.4
CSTR (2)	0.16	0.84	1.2
CSTR (3)	0.14	0.86	1.0
CSTR (4)	0.10	0.90	6.0
CSTR (5)	0.09	0.91	5.5
CSTR (6)	0.08	0.92	5.0
CSTR (7)	0.11	0.89	6.1
CSTR (8)	0.10	0.90	5.5
CSTR (9)	0.09	0.91	5.0
CSTR (10)	0.09	0.91	5.9
CSTR (11)	0.08	0.92	5.4
CSTR (12)	0.08	0.92	5.0

References

[1] B. Buesser, A. J. Gröhn, S. E. Pratsinis, Sintering Rate and Mechanism of TiO_2 Nanoparticles by Molecular Dynamics, The Journal of Physical Chemistry C 115 (2011) 11030–11035. doi:10.1021/jp2032302.

[2] H. K. Park, K. Y. Park, Control of Particle Morphology and Size in Vapor-Phase Synthesis of Titania, Silica and Alumina Nanoparticles, KONA Powder and Particle Journal 32 (2015) 85–101. doi:10.14356/kona.2015018.

[3] S. Li, Y. Ren, P. Biswas, S. D. Tse, Flame aerosol synthesis of nanostructured materials and functional devices: Processing, modeling, and diagnostics, Progress in Energy and Combustion Science 55 (2016) 1–59. doi:10.1016/j.pecs.2016.04.002.

[4] G. Auer, P. Woditsch, A. Westerhaus, J. Kischkewitz, W.-D. Griebler, M. Rohe, M. Liedekerke, Pigments, Inorganic, 2. White pigments, Ullmann's Encyclopedia of Industrial Chemistry (2017) 1–36. doi:{10.1002/14356007.n20_n01.pub2}.

[5] M. C. Heine, S. E. Pratsinis, Agglomerate TiO_2 Aerosol Dynamics at High Concentrations, Particle & Particle Systems Characterization 24 (2007) 56–65. doi:10.1002/ppsc.200601076.

[6] S.-Y. Lee, S.-J. Park, TiO_2 photocatalyst for water treatment applications, Journal of Industrial and Engineering Chemistry 19 (2013) 1761–1769. doi:10.1016/j.jiec.2013.07.012.

[7] K. Woan, G. Pyrgiotakis, W. Sigmund, Photocatalytic Carbon-Nanotube–TiO_2 Composites, Advanced Materials 21 (2009) 2233–2239. doi:10.1002/adma.200802738.

[8] N. Rahimi, R. A. Pax, E. M. Gray, Review of functional titanium oxides. I: TiO_2 and its modifications, Progress in Solid State Chemistry 44 (2016) 86–105. doi:10.1016/j.progsolidstchem.2016.07.002.

[9] X. Chen, S. S. Mao, Titanium Dioxide Nanomaterials: Synthesis, Properties, Modifications, and Applications, Chemical Reviews 107 (2007) 2891–2959. doi:10.1021/cr0500535.

[10] C. Artelt, H. J. Schmid, W. Peukert, Modelling titania formation at typical industrial process conditions: effect of surface shielding and surface energy on relevant growth mechanisms, Chemical Engineering Science 61 (2006) 18–32. doi:10.1016/j.ces.2004.12.053.

[11] R. N. Ghoshtagore, Mechanism of Heterogeneous Deposition of Thin Film Rutile, Journal of The Electrochemical Society 117 (1970) 529. doi:10.1149/1.2407561.

[12] S. E. Pratsinis, H. Bai, P. Biswas, M. Frenklach, S. V. R. Mastrangelo, Kinetics of Titanium(IV) Chloride Oxidation, Journal of the American Ceramic Society 73 (1990) 2158–2162. doi:10.1111/j.1151-2916.1990.tb05295.x.

[13] S. Tsantilis, H. Kammler, S. Pratsinis, Population balance modeling of flame synthesis of titania nanoparticles, Chemical Engineering Science 57 (2002) 2139–2156. doi:10.1016/S0009-2509(02)00107-0.

[14] R. Hong, Z. Ren, J. Ding, H. Li, Experimental investigation and particle dynamic simulation for synthesizing titania nanoparticles using diffusion flame, Chemical Engineering Journal 108 (2005) 203–212. doi:10.1016/j.cej.2005.02.011.

[15] S. C. Garrick, G. Wang, Modeling and simulation of titanium dioxide nanoparticle synthesis with finite-rate sintering in planar jets, Journal of Nanoparticle Research 13 (2011) 973–984. doi:10.1007/s11051-010-0097-x.

[16] M. Y. Manuputty, C. S. Lindberg, M. L. Botero, J. Akroyd, M. Kraft, Detailed characterisation of TiO_2 nano-aggregate morphology using TEM image analysis, Journal of Aerosol Science 133 (2019) 96–112. doi:10.1016/j.jaerosci.2019.04.012.

[17] M. K. Akhtar, Y. Xiong, S. E. Pratsinis, Vapor synthesis of titania powder by titanium tetrachloride oxidation, Journal of Aerosol Science 22 (1991) S35–S38. doi:10.1016/S0021-8502(05)80028-X.

[18] T. Seto, M. Shimada, K. Okuyama, Evaluation of Sintering of Nanometer-Sized Titania Using Aerosol Method, Aerosol Science and Technology 23 (1995) 183–200. doi:10.1080/02786829508965303.

[19] C. S. Lindberg, M. Y. Manuputty, J. Akroyd, M. Kraft, A two-step simulation methodology for modelling stagnation flame synthesised aggregate nanoparticles, Combustion and Flame 202 (2019) 143–153. doi:10.1016/j.combustflame.2019.01.010.

[20] S. E. Pratsinis, P. T. Spicer, Competition between gas phase and surface oxidation of $TiCl_4$ during synthesis of TiO_2 particles, Chemical Engineering Science 53 (1998) 1861–1868. doi:10.1016/S0009-2509(98)00026-8.

[21] Y. Xiong, S. E. Pratsinis, Formation of agglomerate particles by coagulation and sintering – Part I. A two-dimensional solution of the population balance equation, Journal of Aerosol Science 24 (1993) 283–300. doi:10.1016/0021-8502(93)90003-R.

[22] M. Sander, R. H. West, M. S. Celnik, M. Kraft, A Detailed Model for the Sintering of Polydispersed Nanoparticle Agglomerates, Aerosol Science and Technology 43 (2009) 978–989. doi:10.1080/02786820903092416.

[23] C. S. Lindberg, M. Y. Manuputty, E. K. Yapp, J. Akroyd, R. Xu, M. Kraft, A detailed particle model for polydisperse aggregate particles, Journal of Computational Physics 397 (2019) 108799. doi:10.1016/j.jcp.2019.06.074.

[24] M. Kraft, Modelling of Particulate Processes, KONA Powder and Particle Journal 23 (2005) 18–35. doi:10.14356/kona.2005007.

[25] W. J. Menz, M. Kraft, The Suitability of Particle Models in Capturing Aggregate Structure and Polydispersity, Aerosol Science and Technology 47 (2013) 734–745. doi:10.1080/02786826.2013.788244.

[26] M. Frenklach, S. J. Harris, Aerosol dynamics modeling using the method of moments, Journal of Colloid and Interface Science 118 (1987) 252–261. doi:10.1016/0021-9797(87)90454-1.

[27] M. Y. Manuputty, J. Akroyd, S. Mosbach, M. Kraft, Modelling TiO_2 formation in a stagnation flame using method of moments with interpolative closure, Combustion and Flame 178 (2017) 135–147. doi:10.1016/j.combustflame.2017.01.005.

[28] D. L. Marchisio, R. O. Fox, Solution of population balance equations using the direct quadrature method of moments, Journal of Aerosol Science 36 (2005) 43–73. doi:10.1016/j.jaerosci.2004.07.009.

[29] M. J. Hounslow, R. L. Ryall, V. R. Marshall, A discretized population balance for nucleation, growth, and aggregation, AIChE Journal 34 (1988) 1821–1832. doi:10.1002/aic.690341108.

[30] S. Kumar, D. Ramkrishna, On the solution of population balance equations by discretization–I. A fixed pivot technique, Chemical Engineering Science 51 (1996) 1311–1332. doi:10.1016/0009-2509(96)88489-2.

[31] S. Tsantilis, S. E. Pratsinis, Evolution of primary and aggregate particle-size distributions by coagulation and sintering, AIChE Journal 46 (2000) 407–415. doi:10.1002/aic.690460218.

[32] M. K. Akhtar, G. G. Lipscomb, S. E. Pratsinis, Monte Carlo Simulation of Particle Coagulation and Sintering, Aerosol Science and Technology 21 (1994) 83–93. doi:10.1080/02786829408959698.

[33] A. Maisels, F. Einar Kruis, H. Fissan, Direct simulation Monte Carlo for simultaneous nucleation, coagulation, and surface growth in dispersed systems, Chemical Engineering Science 59 (2004) 2231–2239. doi:10.1016/j.ces.2004.02.015.

[34] M. S. Celnik, R. I. A. Patterson, M. Kraft, W. Wagner, Coupling a stochastic soot population balance to gas-phase chemistry using operator splitting, Combustion and Flame 148 (2007) 158–176. doi:10.1016/j.combustflame.2006.10.007.

[35] R. I. A. Patterson, W. Wagner, M. Kraft, Stochastic weighted particle methods for population balance equations, Journal of Computational Physics 230 (2011) 7456–7472. doi:10.1016/j.jcp.2011.06.011.

[36] G. Kotalczyk, F. Kruis, A Monte Carlo method for the simulation of coagulation and nucleation based on weighted particles and the concepts of stochastic resolution and merging, Journal of Computational Physics 340 (2017) 276–296. doi:10.1016/j.jcp.2017.03.041.

[37] Z. Xu, H. Zhao, H. Zhao, CFD-population balance Monte Carlo simulation and numerical optimization for flame synthesis of TiO_2 nanoparticles, Proceedings of the Combustion Institute 36 (2017) 1099–1108. doi:10.1016/j.proci.2016.07.008.

[38] D. Ramkrishna, Population balances: Theory and applications to particulate systems in engineering, 1 ed., Academic Press, San Diego, 2000.

[39] S. A. Matveev, D. A. Zheltkov, E. E. Tyrtyshnikov, A. P. Smirnov, Tensor train versus Monte Carlo for the multicomponent Smoluchowski coagulation equation, Journal of Computational Physics 316 (2016) 164–179. doi:10.1016/j.jcp.2016.04.025.

[40] R. H. West, G. J. O. Beran, W. H. Green, M. Kraft, First-Principles Thermo-

chemistry for the Production of TiO_2 from $TiCl_4$, The Journal of Physical Chemistry A 111 (2007) 3560–3565. doi:10.1021/jp0661950.

[41] C. Lindberg, J. Akroyd, M. Kraft, Developing breakage models relating morphological data to the milling behaviour of flame synthesised titania particles, Chemical Engineering Science 166 (2017) 53–65. doi:10.1016/j.ces.2017.03.016.

[42] J. Akroyd, A. J. Smith, R. Shirley, L. R. McGlashan, M. Kraft, A coupled CFD-population balance approach for nanoparticle synthesis in turbulent reacting flows, Chemical Engineering Science 66 (2011) 3792–3805. doi:10.1016/j.ces.2011.05.006.

[43] A. Boje, J. Akroyd, S. Sutcliffe, J. Edwards, M. Kraft, Detailed population balance modelling of TiO_2 synthesis in an industrial reactor, Chemical Engineering Science 164 (2017) 219–231. doi:10.1016/j.ces.2017.02.019.

[44] A. Boje, J. Akroyd, M. Kraft, A hybrid particle-number and particle model for efficient solution of population balance equations, Journal of Computational Physics 389 (2019) 189–218. doi:10.1016/j.jcp.2019.03.033.

[45] H. Babovsky, A hybrid numerical scheme for aerosol dynamics, in: Numerical Mathematics and Advanced Applications, Springer, 2008, pp. 425–432. doi:0.1007/978-3-540-69777-0.

[46] A. Bouaniche, L. Vervisch, P. Domingo, A hybrid stochastic/fixed-sectional method for solving the population balance equation, Chemical Engineering Science 209 (2019) 115198. doi:10.1016/j.ces.2019.115198.

[47] W. J. Menz, J. Akroyd, M. Kraft, Stochastic solution of population balance equations for reactor networks, Journal of Computational Physics 256 (2014) 615–629. doi:10.1016/j.jcp.2013.09.021.

[48] R. H. West, R. A. Shirley, M. Kraft, C. F. Goldsmith, W. H. Green, A detailed kinetic model for combustion synthesis of titania from $TiCl_4$, Combustion and Flame 156 (2009) 1764–1770. doi:10.1016/j.combustflame.2009.04.011.

[49] P. Buerger, J. Akroyd, S. Mosbach, M. Kraft, A systematic method to estimate and validate enthalpies of formation using error-cancelling balanced reactions, Combustion and Flame 187 (2018) 105–121. doi:10.1016/j.combustflame.2017.08.013.

[50] P. Buerger, J. Akroyd, M. Kraft, Extended first-principles thermochemistry for the oxidation of titanium tetrachloride, Combustion and Flame 199 (2019) 441–450. doi:10.1016/j.combustflame.2018.07.021.

[51] D. Nurkowski, A. W. Jasper, J. Akroyd, M. Kraft, Theoretical study of the Ti–Cl bond cleavage reaction in $TiCl_4$, Zeitschrift für Physikalische Chemie 231 (2017) 1489–1506.

[52] S. Shekar, A. J. Smith, W. J. Menz, M. Sander, M. Kraft, A multidimensional population balance model to describe the aerosol synthesis of silica nanoparticles, Journal of Aerosol Science 44 (2012) 83–98. doi:10.1016/j.jaerosci.2011.09.004.

[53] S. Shekar, W. J. Menz, A. J. Smith, M. Kraft, W. Wagner, On a multivariate population balance model to describe the structure and composition of sil-

ica nanoparticles, Computers & Chemical Engineering 43 (2012) 130–147. doi:10.1016/j.compchemeng.2012.04.010.

[54] A. Kobata, K. Kusakabe, S. Morooka, Growth and transformation of TiO_2 crystallites in aerosol reactor, AIChE Journal 37 (1991) 347–359. doi:10.1002/aic.690370305.

[55] K. E. J. Lehtinen, M. R. Zachariah, Effect of coalescence energy release on the temporal shape evolution of nanoparticles, Physical Review B 63 (2001) 205402. doi:10.1103/PhysRevB.63.205402.

[56] H. Zhang, J. F. Banfield, Thermodynamic analysis of phase stability of nanocrystalline titania, Journal of Materials Chemistry 8 (1998) 2073–2076. doi:10.1039/a802619j.

[57] K. E. Lehtinen, M. R. Zachariah, Energy accumulation in nanoparticle collision and coalescence processes, Journal of Aerosol Science 33 (2002) 357–368. doi:10.1016/S0021-8502(01)00177-X.

[58] M. W. Chase, NIST-JANAF Thermochemical Tables, 4th ed., American Institute of Physics, New York, 1998.

[59] A. Eibeck, W. Wagner, An Efficient Stochastic Algorithm for Studying Coagulation Dynamics and Gelation Phenomena, SIAM Journal on Scientific Computing 22 (2000) 802–821. doi:10.1137/S1064827599353488.

[60] R. I. A. Patterson, J. Singh, M. Balthasar, M. Kraft, J. R. Norris, The Linear Process Deferment Algorithm: A new technique for solving population balance equations, SIAM Journal on Scientific Computing 28 (2006) 303–320. doi:10.1137/040618953.

[61] A. K. Jain, R. C. Dubes, Algorithms for clustering data, Prentice-Hall, 1988.

[62] A. Novikov, PyClustering: Data mining library, Journal of Open Source Software 4 (2019) 1230. doi:10.21105/joss.01230.

[63] C. D. Musick, A. H. Reid Jr, L. Zhang, Titanium dioxide nanopowder manufacturing process, 2007. US Patent 7,208,126.

[64] M. L. Eggersdorfer, S. E. Pratsinis, The Structure of Agglomerates Consisting of Polydisperse Particles, Aerosol Science and Technology 46 (2012) 347–353. doi:10.1080/02786826.2011.631956.

[65] M. L. Eggersdorfer, D. Kadau, H. J. Herrmann, S. E. Pratsinis, Aggregate morphology evolution by sintering: Number and diameter of primary particles, Journal of Aerosol Science 46 (2012) 7–19. doi:10.1016/j.jaerosci.2011.11.005.

[66] H. J. Schmid, B. Al-Zaitone, C. Artelt, W. Peukert, Evolution of the fractal dimension for simultaneous coagulation and sintering, Chemical Engineering Science 61 (2006) 293–305. doi:10.1016/j.ces.2004.11.068.

[67] M. Zhou, H. Jiang, Y. Hu, Z. Lu, H. Jiang, C. Li, Evaluation of mixing performance for the industrial-scale radial multiple jets-in-crossflow mixing structure, Chemical Engineering and Processing - Process Intensification 141 (2019) 107534. doi:10.1016/j.cep.2019.107534.

[68] E. V. Kartaev, V. P. Lukashov, S. P. Vashenko, S. M. Aulchenko, O. B. Kovalev, D. V. Sergachev, An Experimental Study of the Synthesis of

Ultrafine Titania Powder in Plasmachemical Flow-Type Reactor, International Journal of Chemical Reactor Engineering 12 (2014) 377–396. doi:10.1515/ijcre-2014-0001.